A NUMERICAL INVESTIGATION OF FREE-FALL SWIRLING GAS ATOMIZATION PROCESS

MOHAMMADREZA HAGHIGHATJOO

A THESIS

IN

THE DEPARTMENT

OF

MECHANICAL, INDUSTRIAL, AND AEROSPACE ENGINEERING

PRESENTED IN PARTIAL FULFILLMENT OF THE REQUIREMENTS

FOR THE DEGREE OF

MASTER OF APPLIED SCIENCE OF MECHANICAL ENGINEERING

CONCORDIA UNIVERSITY

MONTRÉAL, QUÉBEC, CANADA

NOVEMBER 2020

CONCORDIA UNIVERSITY

School of Graduate Studies

This is to certify that the thesis prepared

By: **Mohammadreza Haghighatjoo**

Entitled: **A numerical investigation of free-fall swirling gas atomization process**

and submitted in partial fulfillment of the requirements for the degree of

Master of Applied Science (Mechanical Engineering)

complies with the regulations of this University and meets the accepted standards with respect to originality and quality.

Signed by the final examining committee:

_____ Chair
Dr. Christian Moreau

_____ Internal Examiner
Dr. Christian Moreau

_____ External Examiner
Dr. Attila Michael Zsaki

_____ Supervisor
Dr. Ali Dolatabadi

Approved _____
Dr. Mamoun Medraj, Graduate Program Director

November 30, 2020 _____
Dr. Mourad Debbabi
Dean of Gina Cody School of Engineering & Computer Science

Abstract

A numerical investigation of free-fall swirling gas atomization process

Mohammadreza Haghighatjoo

Gas atomization is a complex multi-physics route in the powder production field. Fine spherical metal powders can be produced using this technique via atomizing superheated molten metals. In the powder production industry, free-fall gas atomizer is often used for the melt atomization. The most significant advantage of using this type of atomizer is that it avoids melt build-up in the vicinity of gas and melt nozzle exits; the problem which is much more pronounced in the close-coupled gas atomizers. Obtaining smaller particle median diameter (d_{50}) and narrower particle size distribution (PSD) have been the major manufacturing challenge. In the present work, a numerical parametric study is carried out on the atomization process variables of a novel layout of free-fall atomizer in order to reduce d_{50} and narrow down PSD. The used free-fall atomizer features a swirl motion of gas stream which allows the breakup point of the molten jet to be located at a closer distance to the die and benefits the most from the kinetic energy of the gas jets. A two-way coupled Eulerian-Lagrangian approach is utilized. Ideal gas law and k-epsilon turbulence model are employed to simulate the gas flow. In addition, the adaptive mesh refinement (AMR) technique is used to refine the computational domain locally and model the supersonic jet flow more accurately. The number of cells in the domain reaches around 40 million, and five to six shock diamonds are captured using this technique. To model the discrete (particulate) phase, the effects of Reynolds, Mach, and Knudsen numbers on the drag coefficient and Nusselt number on heat transfer are included. Moreover, Kelvin-Helmholtz Rayleigh-Taylor (KHRT) breakup model is used to simulate the molten metal atomization process. It is found that under the same operating condition, the increase in gas to melt ratio (GMR) and number of

nozzles result in a smaller d_{50} and narrower PSD. This numerical analysis also investigates the effect of change in a range of radial and swirl angles. It is observed that increasing the radial angle and decreasing the swirl angle could narrow down the particle size distribution and reduce the particle median diameter.

Acknowledgments

Hereby, I wish to express my sincere gratitude to my dear supervisor Prof. Ali Dolatabadi for his persistent help and encouragement in this research. The goal of this thesis would not have been realized without his continuous supports and insightful comments. I am so grateful to have had such a knowledgeable, considerate, and outstanding supervisor.

Besides, I would like to express my very profound appreciation to my family, in particular my mom and dad whose love and guidance are always with me in pursuing my dreams. Special thanks to my company, Diana for her inspirations and emotional supports. This accomplishment would not have been possible without them.

I also wish to acknowledge my team lead and friend, Dr. Mehdi Jadidi for his enormous help and technical supports whenever I have encountered an issue.

Last but not least, special thanks to all my fellow lab mates at Concordia University especially Saeed Garmeh for his massive supports. Thank you to my friends Nasrin, Hamed, Masoud, Diego, Seyyed Mohammad, and Mohammadreza for providing me with unfailing support and continuous encouragement throughout my years of study.

Contents

List of Figures

List of Tables

List of symbols

T	Temperature	[K]
m	Mass	[kg]
P	Pressure	[Pa]
V	Volume	[m^3]
A	Surface area	[m^2]
g	Gravitational acceleration	[m/s^2]
u	Velocity vector	[m/s]
U_{rel}	Relative velocity vector	[m/s]
d_p	Particle diameter	[m]
d_{50}	Particle median diameter	[m]
K	Thermal conductivity	[W/m.K]
C	Specific heat	[kJ/kg]
H	Latent heat of solidification	[kJ/kg]
k	Turbulence kinetic energy	[J/kg]
ε	Turbulence dissipation rate	[J/kg.s]
ρ	Density	[kg/m^3]
μ	Dynamic viscosity	[kg/m.s]
ν	Kinematic viscosity	[m$^2/s$]
σ	Droplet surface tension	[N/m]
α	Radial angle	Degree

β	Swirl angel	Degree
R_g	Universal gas constant	[J/kg.K]
t	Time	[s]
τ_r	Droplet\particle relaxation time	[s]
D_T	Thermophoretic coefficient	[kg.m$^2/s^2$]
γ	Specific heat ratio	
C_d	Drag coefficient	
Ma	Mach number	
Re	Reynolds number	
We	Weber number	
Pr	Prandtle number	
Nu	Nusselt number	
Kn	Knudsen number	

Chapter 1

Introduction

Overview

In this chapter, a brief introduction to gas atomization process is provided and two leading techniques of this complicated process are described and compared with each other. Besides, a novel design of free-fall gas atomization technique, free-fall swirling gas atomizer is explained in detail. At the end, objectives and significance of this investigation are presented.

1.1 Background

Metal powders are defined as metal or alloy particles in the size range 0.1 to 1000 μm. In a broad range of industrial applications, metal powders are significantly important due to their unique properties and characteristics [1]. Over recent years, the demand for high-quality metal powders has increased dramatically. Therefore, so many works have been conducted in industry and academia to develop different techniques for the metal powder fabrication. Figure 1.1 illustrates a number of standard techniques in the powder production industry [2], which can also be classified into three principal methods: physical, mechanical and chemical [3]. The choice of powder fabrication method is made based on the properties of material and process economics. In other words, there is a relation between the powder production technique and the size, shape, microstructure, and chemistry of product [1].

Metal powders as the basis of the powder processing industry have been employed in a large variety of applications, including powder metallurgy (PM), additive manufacturing (AM), surface engineering, and so forth [4, 5]. Today's applications often need highly spherical powders owing to better flow characteristics and dense packing [6]. Besides, new applications mostly require powders with finer particle median size, narrower particle size distribution (PSD), and higher levels of purity. To meet these requirements, a considerable attention has been paid to the development of equipment that is used to produce fine spherical metal powders [4, 7]. Table 1.1 displays the diameters of powders produced through different approaches.

Atomization process is one of the most common techniques for the metal powder fabrication, which is simply defined as the breakup of a liquid into droplets. Any material in the molten state can be considered for the atomization process [8]. As shown in the subdivision of the

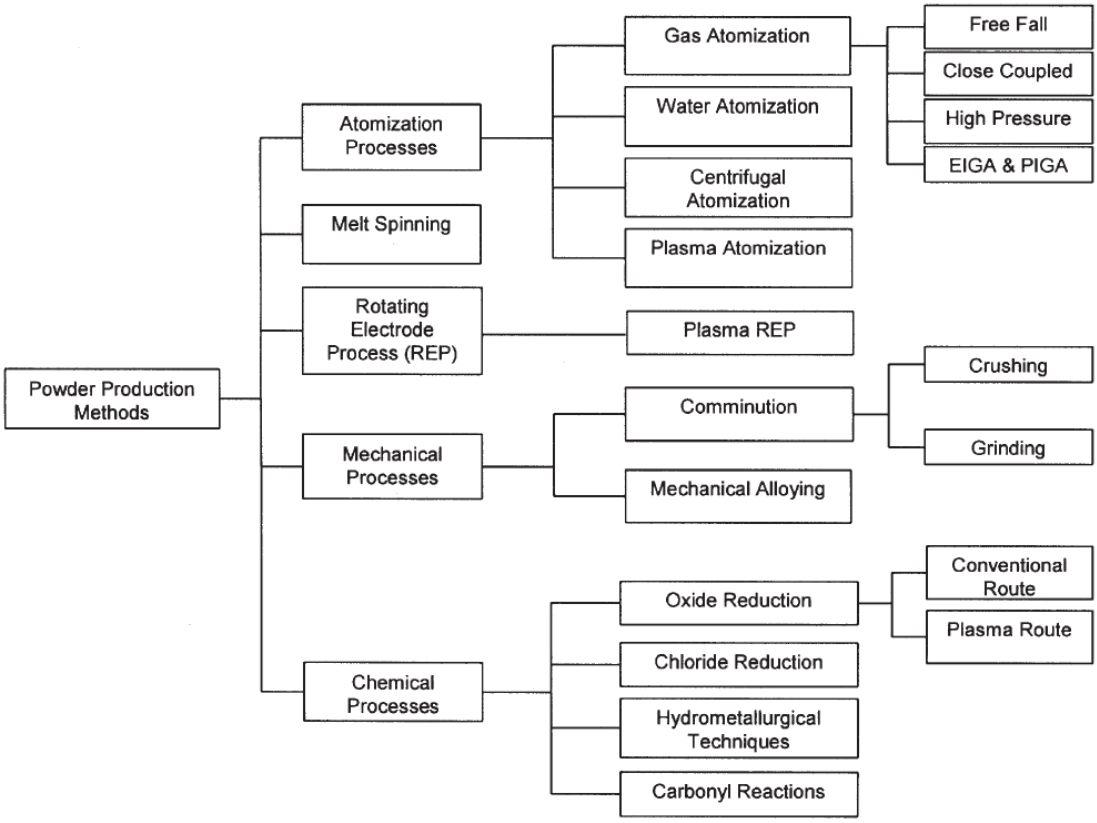

Figure 1.1: Different processes for the metal powder fabrication [2].

Process	Product diameter (μm)	Produced powder
Gas atomization	60-125	Nickel superalloy (IN 100), Ti, Zr, Ti-Al, Fe-Gd, Zn, and Pb
Water atomization	12-16	Fe and Cu
Centrifugal atomization	7-8	Al-20Si
Plasma atomization	40-90	Ti, Mo, Cu, and IN718 (Nickel superalloy)
Plasma-rotating electrode	75-200	1018 steel
Stamp mill, ball mill	25-500	Al, Cu
Oxide reduction	1-10	Fe, Co, Cu, Mo, Al, and Mg
Carbonyl reactions	10	Fe, Ni
Hydrometallurgical techniques	1-10	Ni

Table 1.1: Diameter range of different powders produced by various methods [2].

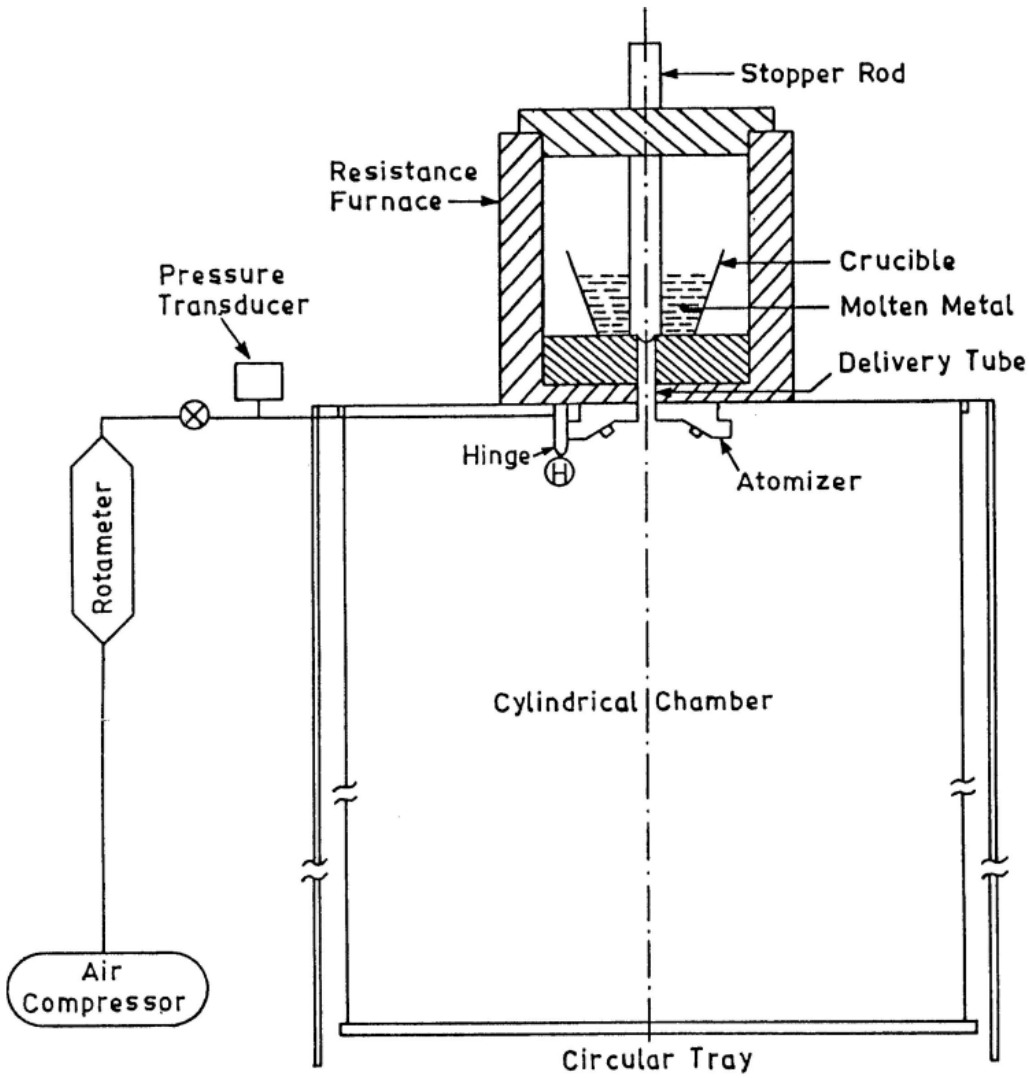

Figure 1.2: Schematic representation of a typical atomization unit [9].

atomization process technique in Fig. 1.1, the fragmentation of the liquid metal into discrete droplets can be carried out by impingement of either gas or water, termed as two-fluid atomization. The practical applications of atomization process can be subdivided into two major fields: spray deposition and powder production [1]. The spray deposition area is out of the scope of this investigation. Figure 1.2 displays a schematic illustration of a typical atomization unit.

Among a broad range of engineering techniques in the atomization process for the production of fine spherical metal powders, gas atomization is the most widely used method [10, 11].

This approach has a great potential for mass production and is a reliable option for the metal powder fabrication due to the versatility, quality, and purity of obtained powders [12]. The gas atomization is defined as a complex multi-physics process that involves the interaction between high-velocity gas flow (gas phase) and melt droplet formation (liquid phase) [13]. Through the atomization mechanism, the central superheated molten metal stream is impinged by high-velocity gas jets, by which the fragmentation of melt stream into fine droplets occurs [8, 14]. Indeed, the gas atomization process creates a notably increased gas-liquid interface in the dispersed multiphase medium [15]. There are intense exchanges of momentum and heat between the gas and liquid phases, leading to an increase in high cooling rates and deep under-cooling of the disintegrated metal droplets [16, 17]. Despite the long history of metal powder production and remarkable development in this area, having a controlled gas atomization process is still challenging and desirable for both academic and industrial aspects [18].

1.2 Literature review

1.2.1 Close-coupled vs free-fall gas atomizer

In the powder production industry, two main methods of gas atomization approach are used, confined, termed as close-coupled and open-die, known as free-fall [2, 7]. In Fig. 1.3, a schematic representation of conventional free-fall arrangement is compared with the close-coupled one. In a close-coupled configuration, the gas exit is confined to the melt delivery tube, in that the melt stream begins to be atomized just below the exit tip of melt feed nozzle. Whereas, in a free-fall arrangement, the molten metal emerging from a reservoir, falls freely up to a certain distance

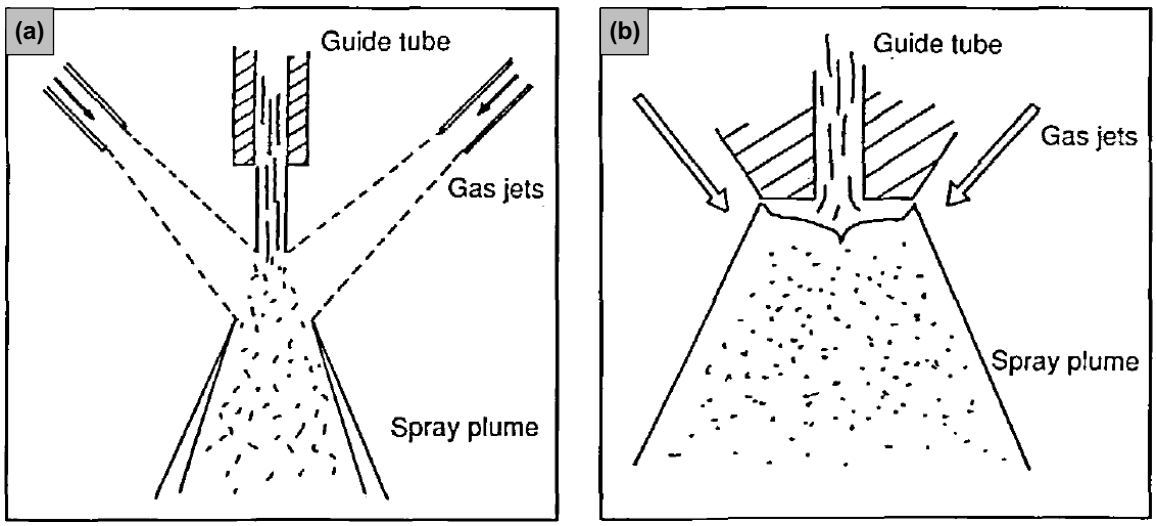

Figure 1.3: Schematic illustration of (a) free-fall and (b) close-coupled gas atomizer configurations [7].

vertically downward before it is impinged by gas flow [8, 19]. The disintegrated droplets, then, get solidified in the gas flow field downstream the geometric point [20]. The point in which gas flow and melt stream meet each other, is technically called geometric or focal point [21]. In the atomization process, the droplets having the size below 500 μm, experience convective cooling and rapid solidification condition [1]. Generally, the gas stream is directed towards the focal point by means of either discrete jets or an annular nozzle slit concentric with the melt stream [7, 22].

In either type of mechanism, fully understanding of kinematical and thermal history of atomized droplets may lead to enhancing the production yield and declining the manufacturing costs [23]. In terms of fine powders with rapid solidification processing (RSP) properties, the close-coupled layout is more likely to yield higher atomization efficiency at identical energy consumption owing to lower distance between the gas and melt exits; whilst, it is more susceptible to reverse flow and splashback of particles [15,24]. Due to the complexity of atomizaion process

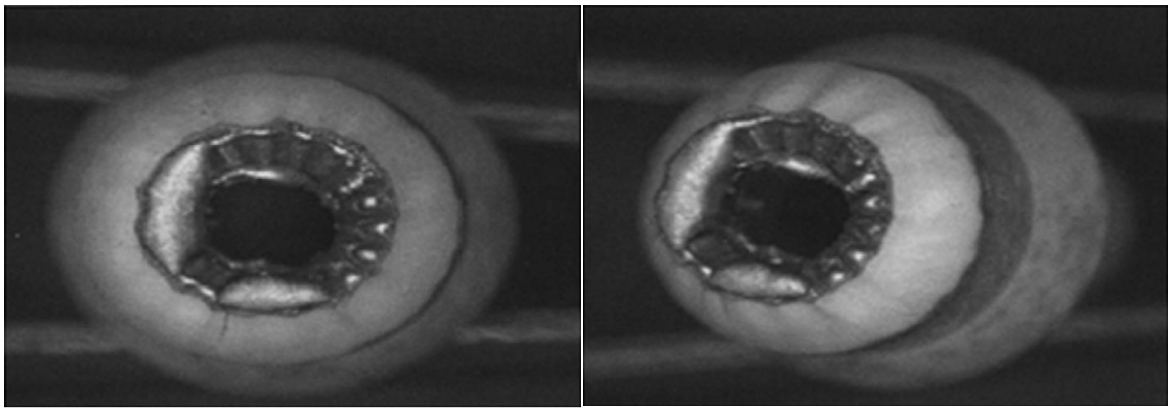

Figure 1.4: A melt delivery nozzle failed owing to melt build-up during gas atomization of Ni-Al [26].

and a deficiency of knowledge regarding gas/molten metal interaction, such problems have not been resolved in the close-coupled arrangement yet [25]. The back-streaming of the melt takes place when the molten metal is drawn back up to the outer surface of melt delivery nozzle and solidified owing to being exposed to the cold expanding gas. The molten metal build-up on the exit plane of melt delivery tube results in changing the size of melt nozzle exit and reducing the melt feed rate. The occurrence of melt freeze-off could ultimately lead metal production process to be aborted [26]. Figure 1.4 shows a melt delivery nozzle which is clogged and failed due to the occurrence of back-streaming phenomenon over the gas atomization process of Ni-Al.

In contrast to the closed-coupled configuration, the free-fall design is not only less problematic in terms of thermal freezing processes of particles, but also much easier to control and regulate the mass flux distribution of droplets in the spray; however, it generates coarser powders [26]. To address this issue and generate finer particles, some solutions such as higher gas flow rate, higher gas-to-melt mass flow rate ratios, and steeper attack angle between the gas and

melt streams, are proposed. These findings are not recommended for raising the yield of manufacturing to the point where the particle median size lies in the range of 5-20 μm, since these solutions are not economical and create an extreme condition. This is the clear reason that the manufacturers abandon this approach for this range of particle median size [7].

Due to the importance of powder size range in the aforementioned industrial applications, this work is focused on a novel design of the free-fall gas atomizer in order to not only benefit the most from the advantages of free-fall type, but also study the possible solutions to generate fine powders. So far, several numerical works have been reviewed and published on the close-coupled atomizers [19,27], while the free-fall atomizers have received less attention numerically [28, 29].

1.2.2 Free-fall gas atomizer

The first study on the gas atomization field was done in 1948 for high-pressure gas atomization (HPGA) method, by which some process variables in the production of aluminum powder like mass flow rate, melt temperature, and gas pressure were investigated [30]. Concerning the free-fall configuration as a method of gas atomization route, several works have been published so far. For the sake of having a parametric study on this type of atomizer, the works which have studied the influence of process variables as well as design factors, are selected to be reviewed. In the literature, the apex angle is called as the angle between the centerline of gas jets in the geometric point and the focal length is named as the distance between the gas nozzle exit and geometric point [21, 31]. Figure 1.5 illustrates the geometric point (G), focal length (F), and apex angle (A) in a typical free-fall gas atomizer.

In the atomization process, the metal powder characteristics can be affected by a broad range

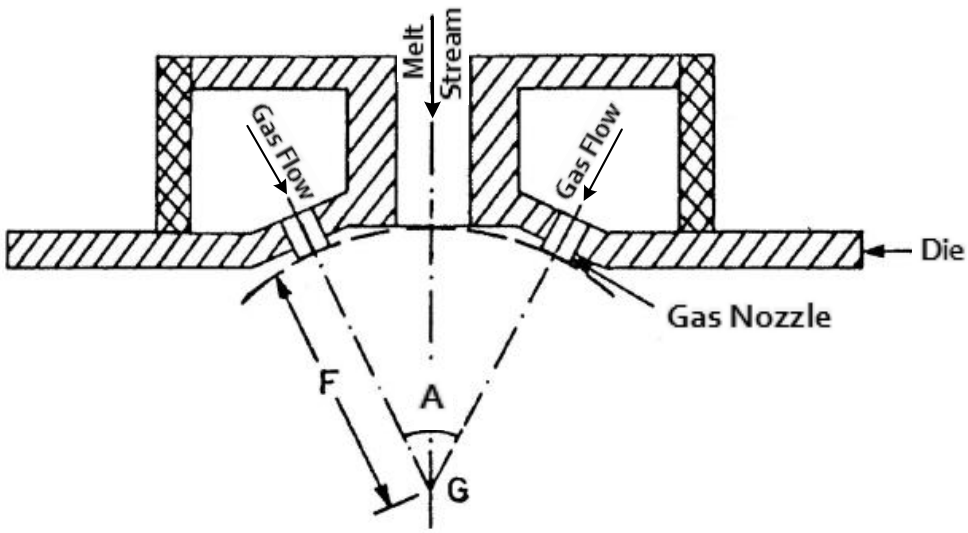

Figure 1.5: Schematic illustration of geometric point, focal length, and apex angle in a typical free-fall gas atomizer (adopted from [9]).

of variables which are classified into two principal categories; first, parameters that are associated with atomization condition and atomizer design, e.g. atomizer geometry, gas nozzle design, melt stream size, metal superheat, and gas pressure of atomization, second, variables which are related to the thermophysical properties of molten metal and the atomizing gas like viscosity, surface tension, density of molten metal and viscosity, density and thermal characteristics of gas [31].

The interaction between freely falling of molten tin and lead with the nitrogen gas was experimentally investigated, in which the gas velocity field around the geometric point was accounted for the atomizers with different apex angles [32]. The gas velocity plays a key role in the efficiency of free-fall atomization process. It has been found that the gas velocity field greatly depends on the back pressure [33, 34] and widely varies in the vicinity of the geometric point. According to the findings of [21], either increase in the diameter of gas nozzle or decrease in the focal length may lead to giving a rise to the gas velocity around the geometric point. To

calculate the gas velocity at or downstream of the geometric point, an empirical correlation is developed [21].

The atomization characteristics are significantly controlled by the atomizing gas pressure [35]. The factor of limiting pressure is introduced to prevent the free-fall atomizers from melt build-up on their bodies. This factor simply states that the free-fall atomizer could be reasonably functional up to a particular limiting pressure [31]. To facilitate the design of free-fall atomizers, a criterion is developed to set the operating pressure during the atomization process [36].

Diverse layouts of free-fall atomizer have been developed and utilized for the disintegration of molten metals. Conventional external mixing free-fall atomizer came up with the combination of two gas nozzle arrangements, named as primary and secondary gas nozzle systems [37]. A further technique, flow-adapted design followed to economize the primary gas use of an external mixing atomizer [38].

1.2.3 Free-fall swirling gas atomizer

Via changing the apex angle and focal length, various atomizers might have been potentially designed and fabricated [21, 31]. Basically, the design of geometric point challenges the atomization operation in such a way that the geometric point is forced to be in a far distance away from the gas nozzles to avoid melt build-up on the atomizer body and allow the atomization to proceed simply. In fact, if the geometric point is placed within close distance to the gas nozzles, the whole amount of melt is not able to pass by the geometric point due to splashing the melt on the gas nozzles and die body. Hence, placing the geometric point in a far distance away from the melt exit is meant a reasonable technique; however, less kinetic energy is transferred to the molten metal, resulting in coarser particle size. It is apparent that the kinetic energy of gas jets

diminishes steadily through axial direction. As a result, the need for benefiting the most from kinetic energy came up with the idea of swirl motion of gas flow which is utilized in the design of high pressure gas atomization route [17]. Swirl flow is formed with an angle that predicts the intensity of flow rotation. This method brings the focal point upward and causes the melt stream to pass after being impinged. Moreover, no melt build-up appears on the gas nozzle shells and it

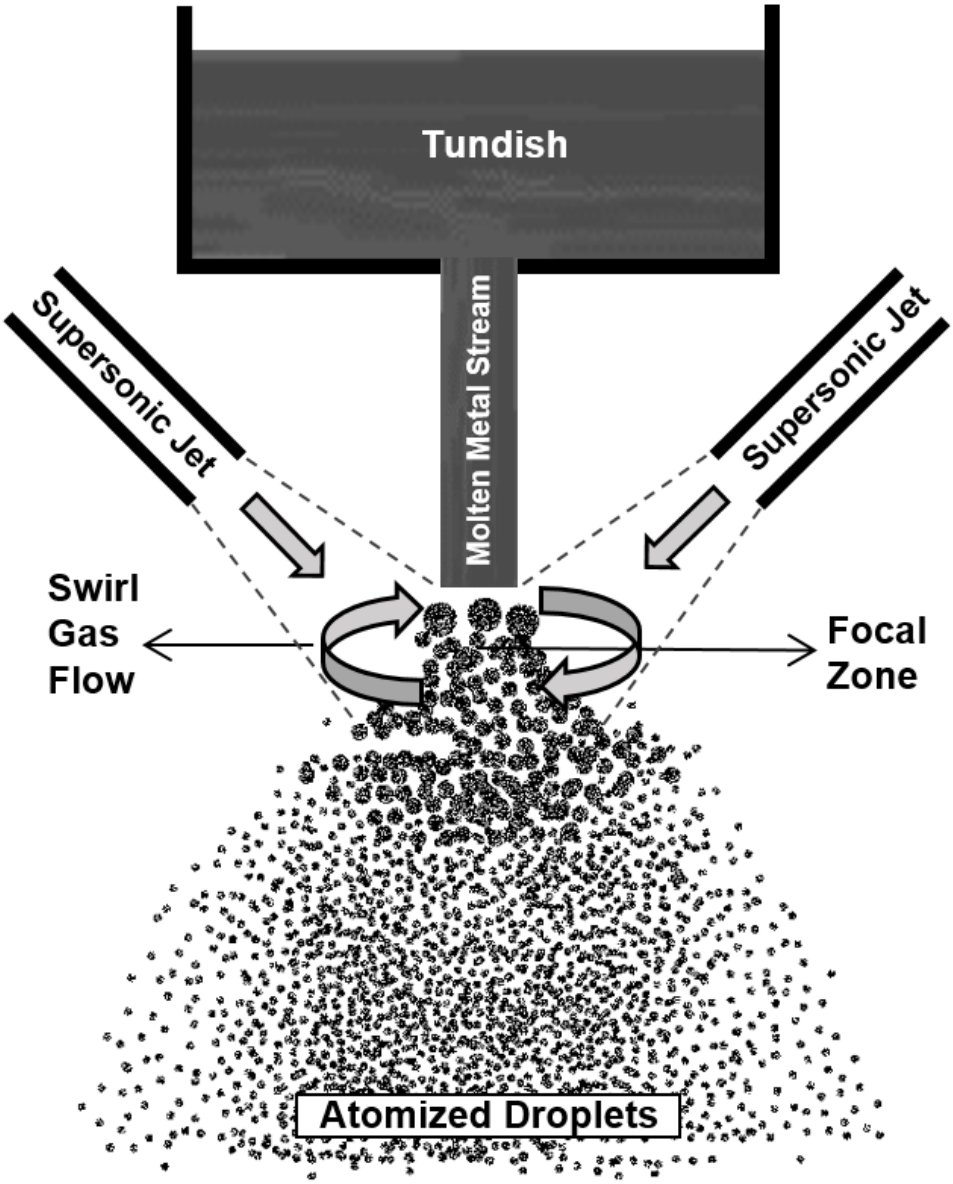

Figure 1.6: The schematic illustration of atomization process in a free-fall swirling gas atomizer.

prevents them to get clogged. The design of free-fall swirling gas atomizer came up with these considerations.

In the conventional layout of free-fall atomizer, the freely falling molten liquid is guided from a reservoir, known as tundish, to the atomization chamber by means of a delivery tube that ends with a converging nozzle, as shown in Fig. 1.2. This nozzle is surrounded by gas jets and situated exactly at the central vertical axis of the whole atomizer. Figure 1.6 depicts the schematic illustration of a free-fall swirling gas atomizer during an atomization process. Via free-fall swirling arrangement, the compressible gas flows supersonic through discrete converging-diverging nozzle and the focal point is substituted by focal zone.

In the free-fall swirling configuration, the discrete gas nozzles are placed outside of the die

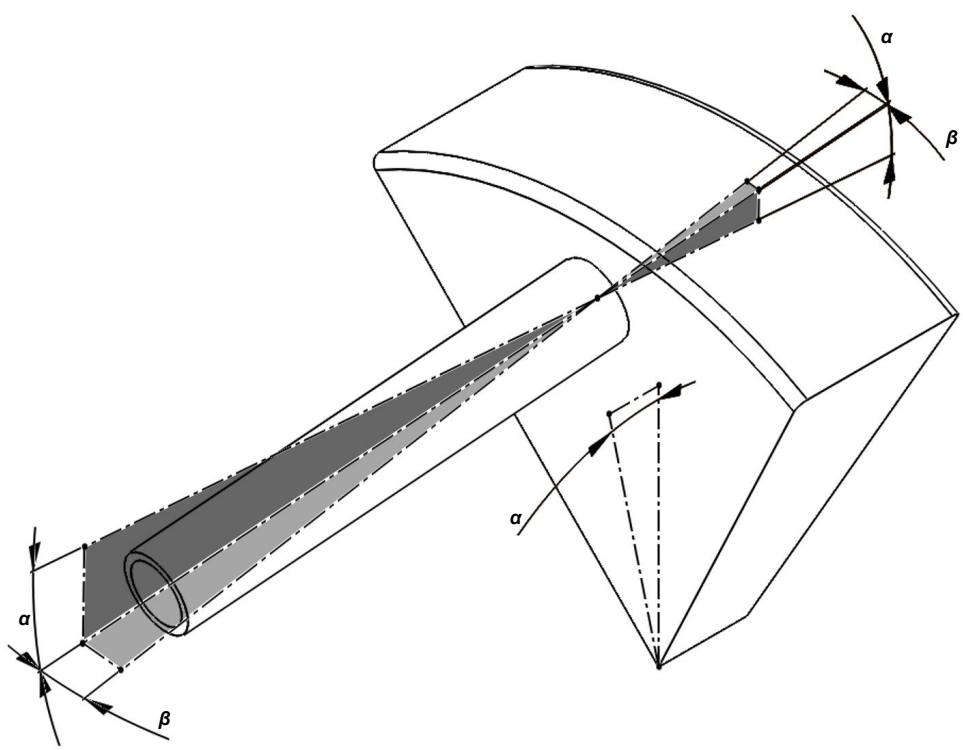

Figure 1.7: The schematic representation of radial (α) and tangential (β) angles in a free-fall swirling die.

body in such a way that they are first positioned inclined towards the central melt stream and then rotated as if the molten liquid is ringed by the gas flow field. In other words, the gas jets are oriented towards the melt flow in two directions, radially and tangentially. As shown in Fig. 1.7, the radial and tangential angles are denoted by α and β, respectively. It should be noted that the tangential angle could be considered as swirl angle as well.

Free-fall swirling gas atmomizer forms a supersonic compressible swirling flow in the dispersed medium. Within this atomizaiton system, the interaction of swirling gas flow with the superheated molten metal is not well-understood yet. This deficiency brings about a serious interest to investigate the effects of gas-to-melt ratio, number of nozzles, and parent droplet size on the particle size distribution during the atomization process. Besides, changing the radial and swirl angles significantly affects the droplet breakup which needs to be studied comprehensively.

1.3 Motivation and objectives

One of the criteria that is taken into consideration for powder quality is particle size distribution [39]. This factor can be characterized by mass median diameter, d_{50}. Presently, the emergence of additive manufacturing into part production area demands high-quality powders which need to meet any pre-defined specifications [17, 18]. Hence, it has been the driven interest in achieving the smaller particle median diameter and narrower particle size distribution in the metal powder production area. The main motivation of the current study is to address the necessity of a numerical work over the free-fall swirling gas atomization process to obtain not only narrower particle size distribution as well as finer particle median diameter, but also a better understanding over the gas dynamic behaviour within such technology.

The objectives of this work are summarized below

- Three-dimensional numerical investigation of the interaction between the compressible supersonic gas jets and the superheated molten metal within the free-fall swirling gas atomization process.

- Study the effect of atomization operating conditions such as back pressure, melt mass flow rate, number of gas nozzles, and parent droplet size on the molten metal breakup, aiming for narrowing down the particle size distribution and reducing the mass median diameter.

- Investigating the impact of design factors like the radial and swirl angles of gas nozzles on in-flight particle characteristics, back flow, and focal point.

Chapter 2

Methodology

Overview

In this chapter, the fundamental physics of atomization process and governing equations for both continuous and dispersed phases are explained. Moreover, all the assumptions, boundary conditions and reasons behind them are discussed in detail. This investigation presents a solution for modeling the gas phase, then this solution is utilized for the liquid phase calculations using the Lagrangian particle tracking approach.

2.1 Continuous phase modelling

Using the commercially available ANSYS-Fluent 2019R2 [40], a three-dimensional simulation of free-fall swirling gas atomizer is undertaken. To provide an inert environment, the nitrogen gas is selected for the operational fluid of continuous phase [1] and modeled as compressible gas using the ideal gas law as equation of state. The remaining properties are provided by the database of the commercial code used.

2.1.1 Geometry and boundary conditions

Figure 2.1 demonstrates the front view of the computational domain with detailed conditions on boundaries. In the industrial scale of atomization system, since the atomized particles require enough time to cool down, the atomization chamber, so-called primary hopper, is built fairly large. Only half a meter of primary hopper in height is taken into consideration due to the restrictions of mesh size and computational costs.

Throughout this study, mass flow inlet is selected for the boundary condition at the inlets of gas nozzles with the room temperature, and the walls of gas nozzles are set as wall at 298 K like the body of the atomizer and the upstream side of cylindrical domain. The remaining sides are considered as pressure outlet at the atmospheric pressure with 100 K above the room temperature since the medium temperature is indeed high in the downstream due to high-temperature in-flight droplets and gas stream. It is noted that the interface between the core and rest of domain, is set as interior and the no-slip condition is considered for the nozzle walls and die body. For the free-fall swirling gas atomizer, a guide tube or sleeve can be considered to transfer the molten

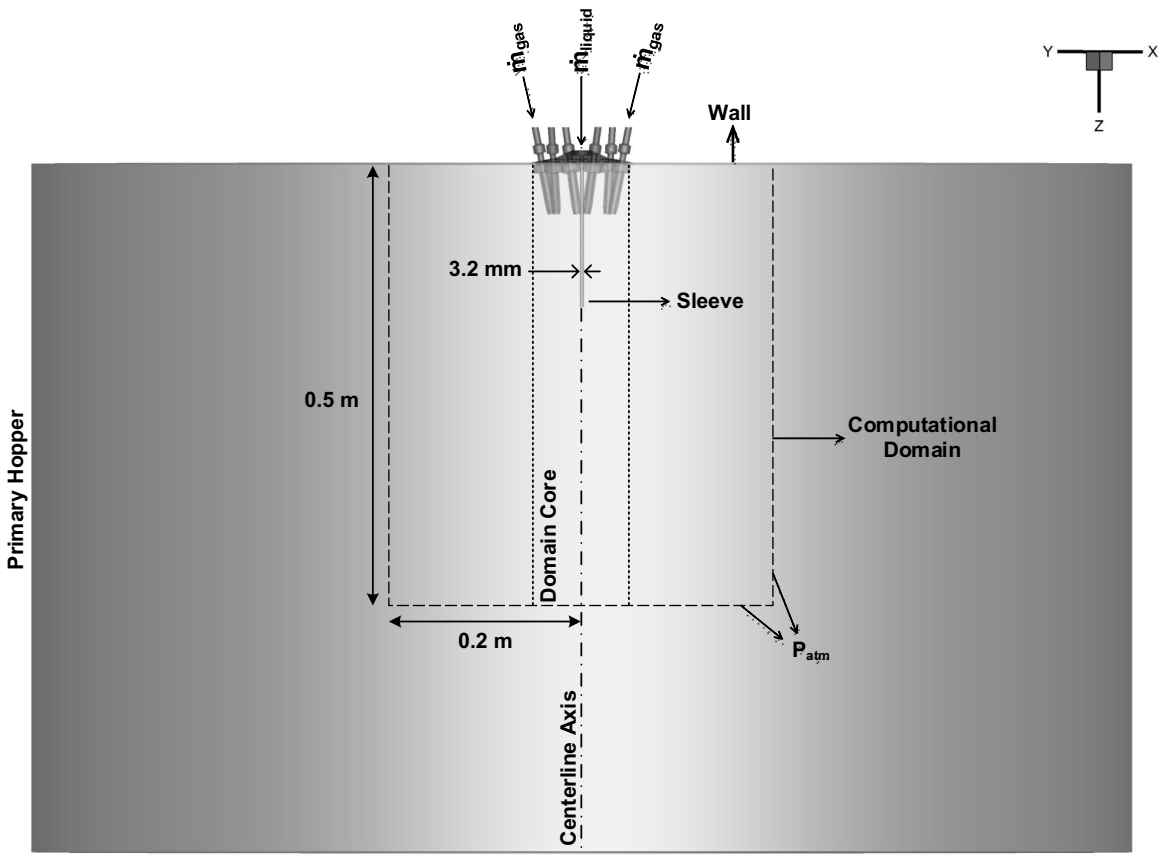

Figure 2.1: An overview of computational domain size, boundary conditions, and primary hopper. It is noted that the sizes are not scaled.

liquid from the melt nozzle of the delivery tube to a distance closer to the atomization zone. The sleeve diameter is the same size of melt nozzle, 3.2 mm.

2.1.2 Governing equations

The continuous phase is considered as a viscous compressible flow, hence, Navier-Stokes equations are used to solve the gas phase flow field. These equations are given as follows.

Conservation of mass equation

The continuity or mass conservation equation is expressed as below,

$$\frac{\partial \rho}{\partial t} + \nabla.(\rho\vec{\nu}) = S_m \tag{2.1}$$

Equation 2.1 shows the general form of continuity equation which is valid for both incompressible and compressible flows. The source term S_m indicates the mass which is added to the continuous phase from the second phase, i.e. dispersed phase [40].

Conservation of momentum equation

The general form of momentum conservation equation for an inertial reference frame is written as follows,

$$\frac{\partial}{\partial t}(\rho\vec{\nu}) + \nabla.(\rho\vec{\nu}\vec{\nu}) = -\nabla p + \nabla.(\bar{\bar{\tau}}) + \rho\vec{g} + \vec{F} \tag{2.2}$$

where p is the static pressure, $\bar{\bar{\tau}}$ is the stress tensor as described below, $\rho\vec{g}$ is the gravitational body force and $\vec{F}$ is the external body forces [40]. Term $\vec{F}$, external body force comes from the interaction between continuous and dispersed phases in this study, which will be discussed in detail in the following.

The parameter $\bar{\bar{\tau}}$ is obtained from,

$$\bar{\bar{\tau}} = \mu\left[\left(\nabla\vec{\nu}^T\right) - \frac{2}{3}\nabla.\vec{\nu}I\right] \tag{2.3}$$

In equation 2.3, μ and I are molecular viscosity and unit tensor, respectively. The second term in the right-hand side explains the impact of volume dilation that considers the variation of volume [41].

Conservation of energy equation

The general form of energy equation is expressed as following,

$$\frac{\partial}{\partial t}(\rho E) + \nabla.(\vec{v}(\rho E + p)) = \nabla.\left(K_{eff}\nabla T + (\bar{\bar{\tau}}_{eff}.\vec{v})\right) + S_h \tag{2.4}$$

where K_{eff} and S_h are effective conductivity and volumetric heat sources, respectively. The first two terms on the right-hand side of equation 2.4 describe energy transfer due to conduction and viscous dissipation, respectively. Also, E is defined as follows [40],

$$E = h - \frac{P}{\rho} + \frac{V^2}{2} \tag{2.5}$$

Equation of state

The following equation, called equation of state for ideal gas, is utilized to take the compressibility effects of gas into account and close the aforementioned equations.

$$p = \rho R T \tag{2.6}$$

$$R = \frac{R_g}{M} \tag{2.7}$$

where R, R_g, and M are specific gas constant for the gas under consideration, universal gas constant, and average molecular mass, respectively [40].

2.1.3 Turbulence model

The compressible gas flows through discrete converging-diverging nozzles and creates a supersonic condition in the exhaust stream of gas nozzles. Due to the high-pressure gradient between the gas nozzle inlets and primary hopper medium during the atomization process, the gas flow undergoes a sudden expansion at the nozzle exit. This expansion results in acceleration of gas flow and generating a turbulence area in the atomization chamber. Turbulence is further affected by the inclusion of molten metal stream in the focal zone. In addition, the gas stream exits with a swirl angle, developing a swirling high-velocity flow field in the atomization chamber. In the free-fall swirling gas atomizer, due to the swirl motion of gas flow, high-pressure gradient, and high-velocity differences, choosing a turbulence model which is able to predict the flow characteristic of such system under these conditions, is of great importance.

Due to the high computational costs associated with DNS and LES, Reynolds averaged Navier-Stokes (RANS) turbulence model has been widely used in simulating the gas atomization process. Among all two-equation and five-equation models of RANS, *k-epsilon* and Reynolds stress models are mostly utilized for atomization applications [20, 26]. The family of *k-epsilon* model needs less computational time compared to Reynolds stress models [40]. In this study, standard *k-epsilon* is chosen to predict the turbulence characteristics of the gas flow due to the robustness, economy, and reasonable accuracy of numerical results.

In the Reynolds-average Navier-Stokes turbulence model, the solution variables of Navier-Stokes equations are decomposed into mean (time-averaged) and fluctuating components. For the velocity, the components are described as below,

$$u_i = \overline{u}_i + \acute{u}_i \tag{2.8}$$

where $\overline{u}_i$ and $\acute{u}_i$ are the mean and fluctuating components of velocity, respectively [40].

Similarly, this approach can be applied for the scalar variables like pressure, as well.

$$\phi = \overline{\phi} + \acute{\phi} \tag{2.9}$$

where ϕ represents a scalar variable like pressure or energy [40].

Reynolds-averaged Navier-Stokes (RANS) equations can be obtained by substituting the flow variables into the instantaneous continuity and momentum equations and talking a time average, expressed as following,

$$\frac{\partial \rho}{\partial t} + \frac{\partial}{\partial x_i}(\rho u_i) = 0 \tag{2.10}$$

$$\frac{\rho}{\partial t}(\rho u_i) + \frac{\partial}{\partial x_j}(\rho u_i u_j) = -\frac{\partial p}{\partial x_i} + \frac{\partial}{\partial x_j}\left[\mu\left(\frac{\partial u_i}{\partial x_j} + \frac{\partial u_j}{\partial x_i} - \frac{2}{3}\delta_{ij}\frac{\partial u_l}{\partial x_l}\right)\right] + \frac{\partial}{\partial x_j}\left(-\rho\overline{\acute{u}_i\acute{u}_j}\right) \tag{2.11}$$

In equation 2.11, the first and second terms on the left-hand side show unsteady and advection, respectively. Also, on the right-hand side, the first term represents pressure gradient, the second term denotes diffusion, and the term $-\rho\overline{\acute{u}_i\acute{u}_j}$ is called Reynolds stresses. To close equation 2.11, the Reynolds stresses which are associated with the velocity gradient, must be modeled. In a common approach, the Reynolds stresses are approximated using Boussinesq hypothesis and written as following,

$$\rho\overline{\acute{u}_i\acute{u}_j} = \mu_t\left(\frac{\partial u_i}{\partial x_j} + \frac{\partial u_j}{\partial x_i}\right) - \frac{2}{3}\left(\rho k + \mu_t\frac{\partial u_k}{\partial x_k}\right)\delta_{ij} \tag{2.12}$$

where μ_t, k and δ_{ij} are turbulent viscosity, turbulence kinetic energy and Dirac delta function, respectively [40]. This approximation is used in *k-epsilon* model to model the Reynolds stresses. For the standard *k-epsilon* model, two separate additional transport equations are solved. The transport equations are turbulence kinetic energy (k) and turbulent dissipation rate (ε). The turbulent viscosity is computed as a function of k and ε.

Transport equations for the standard *k-epsilon* model

The general form of transport equations, turbulence kinetic energy (k) and rate of dissipation (ε) are computed from the following expressions,

$$\frac{\partial}{\partial t}(\rho k) + \frac{\partial}{\partial x_i}(\rho k u_i) = \frac{\partial}{\partial x_j}\left[\left(\mu + \frac{\mu_t}{\sigma_k}\right)\frac{\partial k}{\partial x_j}\right] + G_k + G_b + \rho\varepsilon - Y_M + S_k \tag{2.13}$$

and

$$\frac{\partial}{\partial t}(\rho \varepsilon) + \frac{\partial}{\partial x_i}(\rho \varepsilon u_i) = \frac{\partial}{\partial x_j}\left[\left(\mu + \frac{\mu_t}{\sigma_\varepsilon}\right)\frac{\partial \varepsilon}{\partial x_j}\right] + C_{1\varepsilon}\frac{\varepsilon}{k}\left(G_k + C_{3\varepsilon}G_b\right) - C_{2\varepsilon}\rho\frac{\varepsilon^2}{k} + S_\varepsilon \tag{2.14}$$

In these equations, G_k denotes generation of turbulent kinetic energy from the mean velocity gradients and G_b represents the turbulence kinetic energy generation due to buoyancy. Y_M is the contribution of the fluctuating dilatation in compressible turbulence to the overall dissipation rate. $C_{1\varepsilon}$, $C_{2\varepsilon}$, and $C_{3\varepsilon}$ are constant, and σ_k and σ_ε represent the turbulent Prandtl numbers for k and ε, respectively. To close the transport equations, S_k and S_ε are user-defined source terms for k and ε, respectively. The constants of model have the default values of $C_{1\varepsilon} = 1.44$, $C_{2\varepsilon} = 1.92$,

$\sigma_k = 1.0$, and $\sigma_\varepsilon = 1.3$ [40].

In the standard *k-epsilon* model, similar to other models of *k-epsilon* family, turbulence viscosity is calculated as follows,

$$\mu_t = \rho C_\mu \frac{k^2}{\varepsilon} \tag{2.15}$$

where C_μ is constant and equal to 0.09.

In equations 2.13 and 2.14, the generation of turbulent kinetic energy from the mean velocity gradients and buoyancy are computed as below,

$$G_k = \mu_t S^2 \tag{2.16}$$

$$G_b = -g_i \frac{\mu_t}{\rho Pr_t} \frac{\partial \rho}{\partial x_i} \tag{2.17}$$

where G_b is neglected since the gravity force is not considered in this study.

Also, in the high-Mach-number flows like the present work, the compressibility effect must be inlcuded for the turbulence. This effect is so-called ”dilatation dissipation” and denoted as Y_M. The dilatation dissipation, Y_M is written as below,

$$Y_M = 2\rho\varepsilon {M_t}^2 \tag{2.18}$$

$$M_t = \sqrt{\frac{k}{\gamma R T}} \tag{2.19}$$

where M_t is the turbulent Mach number [40].

Near-wall treatment

In the wall-bounded turbulent flows, the walls have a significant effect on the turbulence behavior of flow. The solution variables of the flow have large gradients near the walls. To maintain the accuracy of the numerical results, modeling the flow near the walls is taken into consideration.

According to the experimental results, the flow in the near-wall region is subdivided into three layers viscous, buffer, and fully-turbulent [40]. As shown in Fig. 2.2, in the closest layer to the wall which is called ”viscous sublayer”, the flow is laminar and the molecular viscosity is the dominant variable in momentum and heat or mass transfer. In the outer layer, called the fully-turbulent layer, turbulent shear plays a dominant role. In between, there is a transitional

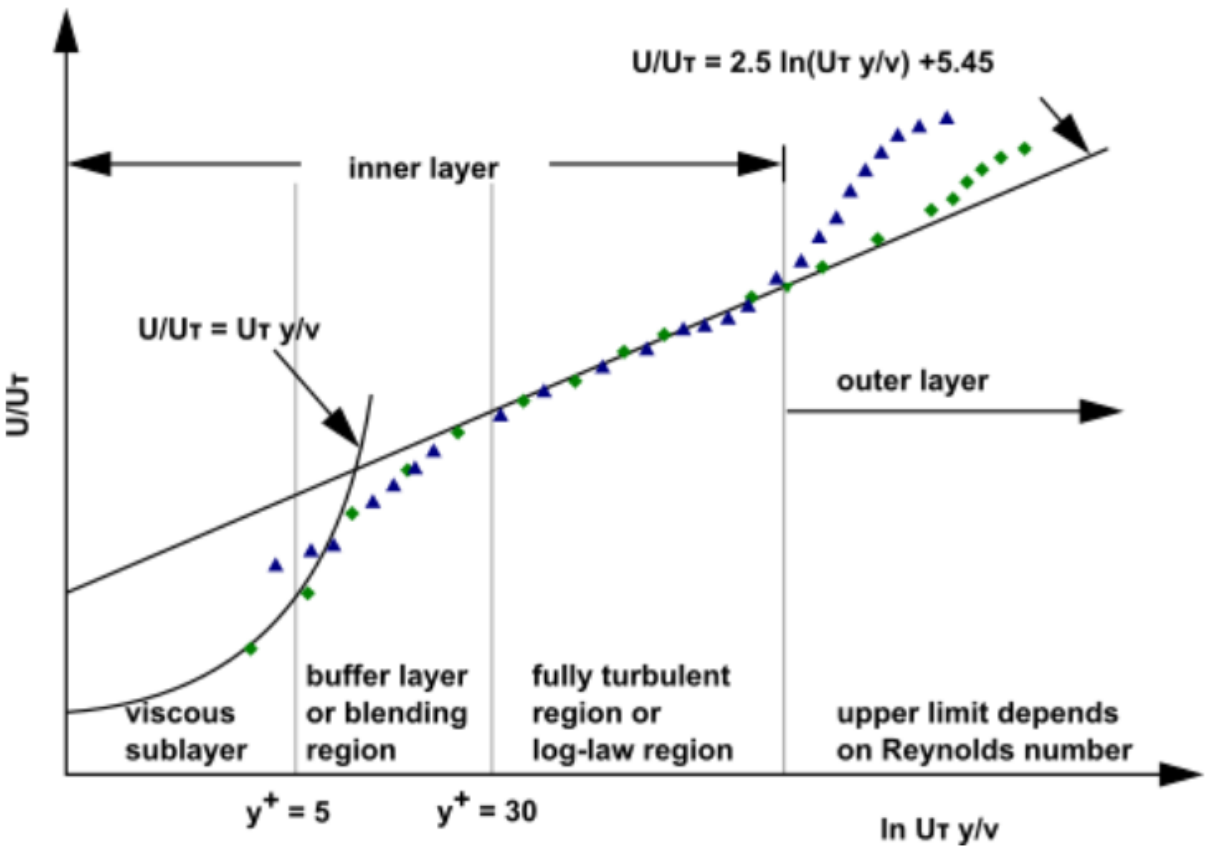

Figure 2.2: Subdivisions of the near-wall region (log-law region of velocity and wall shear stress data) [40].

layer which includes the influence of both molecular and turbulent viscosities [40].

In general, for modeling the near-wall region, there are two models, wall functions and near-wall model. In the wall functions approach, viscous sublayer and buffer layer, called viscosity-affected region, are not resolved. Instead, semi-empirical formulas are employed to bridge the viscosity-affected region between the wall and the fully-turbulent region.

In the near-wall model approach, the viscosity-affected region is resolved by using some modifications in the turbulence models and a mesh all the way to the wall. The turbulence models are valid throughout the near-wall region, unlike the wall functions approach [40]. Figure 2.3 displays a schematic illustration of the differences between these two approaches for the near-wall treatments.

The near-wall model is often used in either low-Reynolds flows or flows with complicated near-wall phenomena. Also, the mesh has to be fine enough near the wall which can impose high computational costs. In the current study, since capturing the flow characteristics near the wall, i.e. in the viscous-affected region, is not of interest, the wall functions approach is applied for the near-wall treatments.

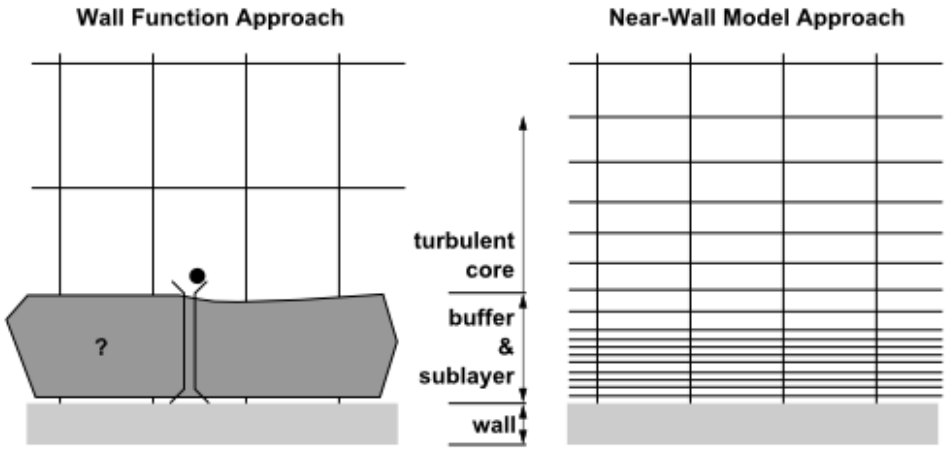

Figure 2.3: A schematic representation of wall functions vs near-wall model approach [40].

Wall functions

According to the wall functions approach, the law-of-the-wall for the mean velocity is given as below,

$$U^* = \frac{1}{K} ln(Ey^*) \qquad y^* > 11.225 \tag{2.20}$$

$$U^* = y^* \qquad y^* < 11.225 \tag{2.21}$$

where *K* is Von Karman constant (=0.4187) and *E* is empirical constant (=9.793). The parameters U^* and y^* are the dimensionless velocity and the dimensionless distance of the element from the wall, respectively, computed as following [40],

$$U^* \equiv \frac{U_P C_\mu^{\frac{1}{4}} k_P^{\frac{1}{2}}}{\frac{\tau_w}{\rho}} \tag{2.22}$$

$$Y^* \equiv \frac{\rho C_\mu^{\frac{1}{4}} k_p^{\frac{1}{2}} y_P}{\mu} \tag{2.23}$$

where U_P and k_P are mean velocity of the fluid and turbulence kinetic energy at the wall-adjacent cell centroid, *P*, respectively. Also, y_P shows the distance from the centroid of the wall-adjacent cell to the wall, *P* and μ is the dynamic viscosity of the fluid.

For highly compressible flows, the temperature distribution in the near-wall region differs greatly from that of low subsonic flows, owing to the viscous dissipation heating. The law-of-the-wall is applied for the non-dimensional temperature and written as below [40],

$$T^* \equiv \frac{(T_w - T_P)\rho c_P C_\mu^{\frac{1}{4}} k_p^{\frac{1}{2}}}{\dot{q}} \tag{2.24}$$

$$T^* = Pry^* + \frac{1}{2}\rho Pr \frac{C_\mu^{\frac{1}{4}} k_p^{\frac{1}{2}}}{\dot{q}} {U_P}^2 \qquad y^* < y_t^* \tag{2.25}$$

$$T^* = Pr_t \left[\frac{1}{K} ln(Ey^*) + P\right] + \frac{1}{2}\rho \frac{C_\mu^{\frac{1}{4}} k_p^{\frac{1}{2}}}{\dot{q}} \left[Pr_t {U_P}^2 + (Pr - Pr_t){U_c}^2\right] \qquad y^* > y_t^* \tag{2.26}$$

where $\dot{q}$, c_P, and k_P are wall heat flux, specific heat of the fluid, and turbulent kinetic energy at the wall-adjacent cell centroid, respectively. The parameters T_P and T_w represent the temperatures at the wall-adjacent cell centroid and wall, respectively. Also, Pr is molecular Prandtl number, Pr_t is turbulent Prandtl number (0.85 at the wall), and U_c is mean velocity magnitude at $y^* = {y_t}^*$. The parameter *P* in equation 2.26 can be obtained from

$$P = 9.24 \left[\left(\frac{Pr}{Pr_t}\right)^{\frac{3}{4}} - 1\right] [1 + 0.28e^{-0.007Pr/Pr_t}] \tag{2.27}$$

In equations 2.25 and 2.26, the compressibility effects are taken into consideration with the second term of the right-hand side of each equation [40].

2.1.4 Numerical technique

The governing equations are solved based on the finite volume method (FVM) using ANSYS-Fluent 2019R2. The finite volume method uses a control-volume-based technique to subdivide the domain into discrete control volumes and solve the governing equations using the computational mesh. The pressure-based approach is selected for the solver and the Navier-Stokes equations, including the conservation of mass, momentum, and energy are discretized by the SIMPLE algorithm. In the pressure-based solver, a solution algorithm is employed to solve the governing equations sequentially, meaning the equations are segregated from one another. A solution loop for the segregated pressure-based is displayed in Fig. 2.4. For the sake of accuracy,

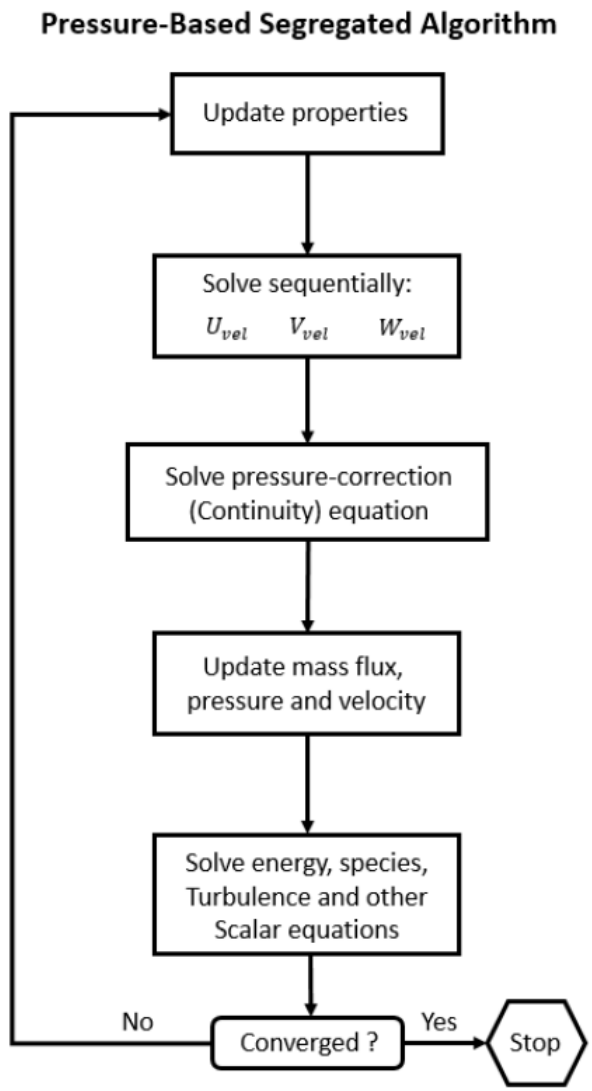

Figure 2.4: Solution algorithm for the pressure-based segregated solver [40].

second order upwind scheme is considered for the continuity, momentum, and energy [40].

2.1.5 Mesh independence analysis

As regards the complexity of free-fall swirling atomizer geometry and the necessity of producing a three-dimensional fine grid, the mesh generation of computational domain is performed in two steps; first, a conformal hybrid mesh is created across the entire domain, then, the domain core

is partially refined in terms of gas stream characteristics.

In the hybrid mesh generation step, meshing the domain core is done by the robust unstructured technique using all tetrahedron elements. In the outside of domain core, owing to the large size of this portion, a structured mesh is generated via hexahedron elements in order to minimize the mesh size significantly. The structured and unstructured meshes, afterwards, are integrated by the pyramid elements. Figure 2.5 (a) displays a cut plane of hybrid mesh resolution produced in the first step.

Since the gas velocity plays a significant role in the atomization process and higher gas velocity could lead to producing a powder with smaller size [13], capturing the whole shock diamonds of supersonic compressible flow is critical and of interest. To do so, the resulting 8-million-cell

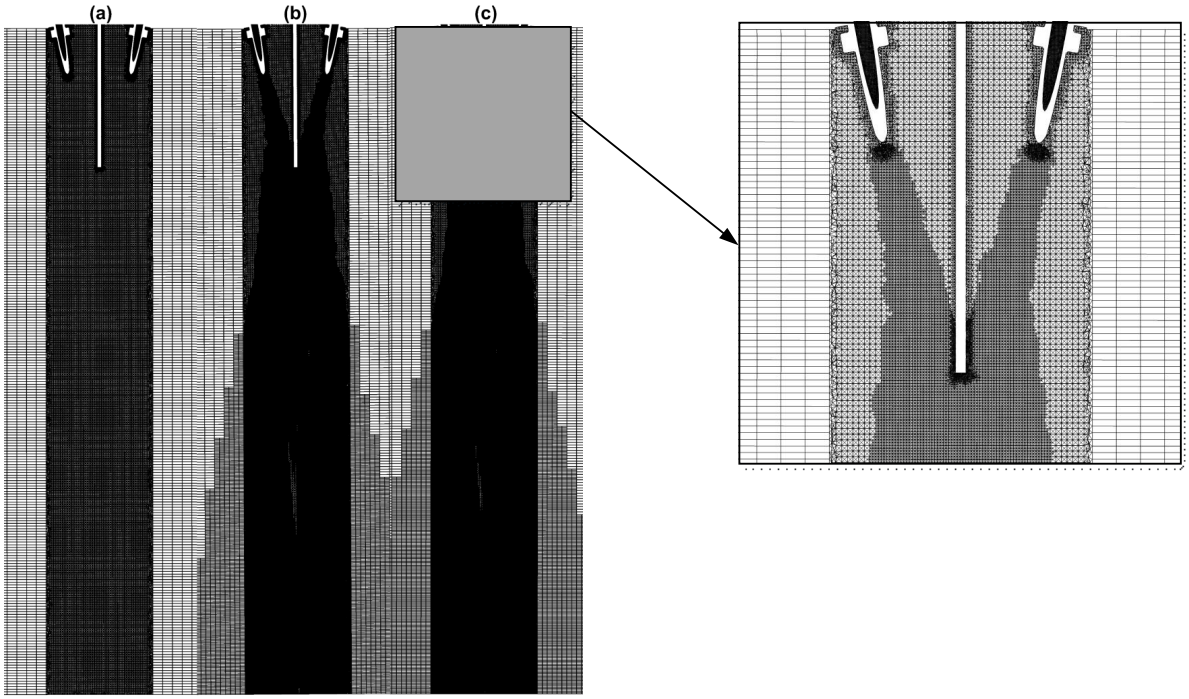

Figure 2.5: Mesh resolution of (a) hybrid-no adaptive refinement (b) hybrid-adaptive refinement-refine threshold=0.0007 (c) hybrid-adaptive refinement-refine threshold=0.0005 (with zoom-in view).

hybrid grid from the first step is refined by the adaptive mesh refinement option of the ANSYS-Fluent solver to make a 40-million-cell refined mesh. By using the gradient approach, the mesh refinement is performed up to 3-level and due to the presence of highly compressible gas flow, the density variable is chosen for the gradient method. The refine threshold is studied up to 0.0005, aiming for the refinement of the whole domain core. The refine threshold is set to refine the cells with density gradient values above this threshold [40].

Figure 2.5 shows various grid resolutions produced over each step. Despite the minor difference between the mesh sizes of thresholds 0.0007 and 0.0005, the features of shock diamonds are better captured by the threshold 0.0005, in particular the last weak shock diamond which is

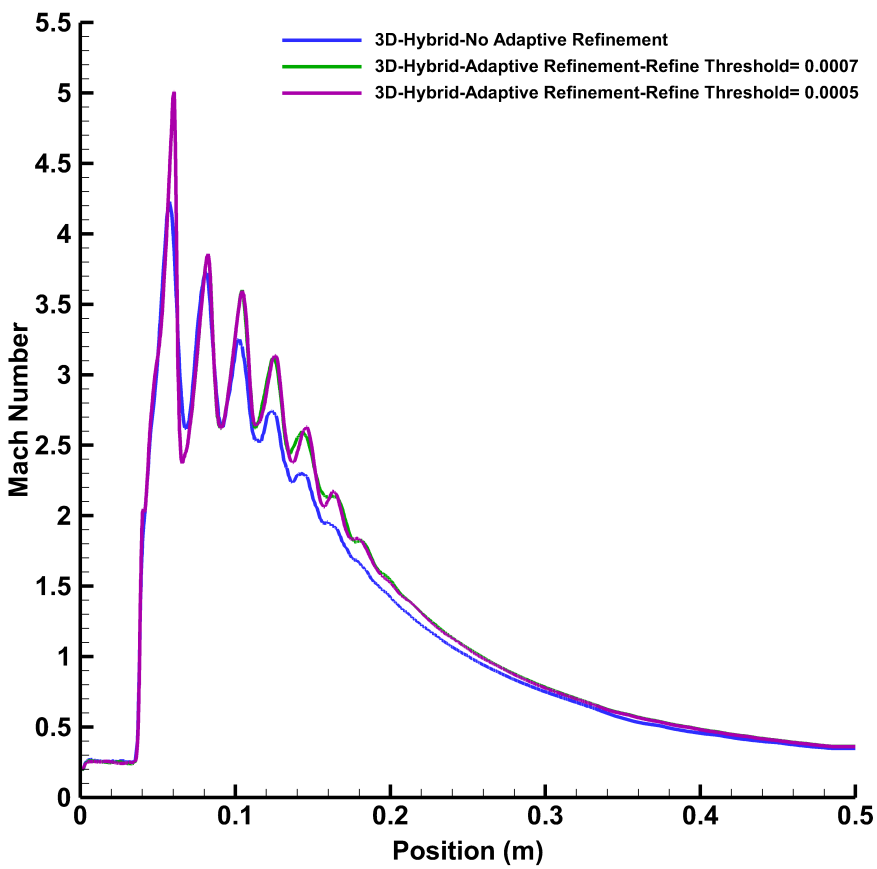

Figure 2.6: Variation of Mach number along the centerline of gas nozzle over various mesh qualities.

situated in the vicinity of the atomization focal zone, as shown in Fig. 2.6. Furthermore, Fig. 2.6 demonstrates that the Mach number of adaptive mesh refinement technique differs extremely from the initial coarse hybrid grid to an extent of roughly 20% in some points. Consequently, in the present work, the hybrid adaptive refined mesh with the refine threshold of 0.0005 is utilized for the numerical simulation.

2.2 Dispersed phase modelling

After modeling the gas flow, the converged solution of continuous phase is used to obtain a solution for the dispersed phase by injecting particles into the computed flow field. The existing gas flow could interact with the injected particles by the exchange of mass, momentum, and energy.

For the dispersed phase, nickel is used as the molten metal whose thermophysical properties are listed in table 2.1. Generally, the melt stream is injected superheated from 75 to 150 K during the atomization process [1]. In this study, the melt superheat is considered 100 K above the melting point with the mass flow rate of 8 kg/min from the central axis of die. Discrete

Property	Unit	Value	Reference
Density	kg/m^3	7810	[42]
Melting point	K	1728	[42]
Thermal conductivity	W/m K	60	[43]
Viscosity	kg/m s	0.0046	[43]
Thermophoretic coefficient	$kg\ m^2/s^2$	Talbot-diffusion-coeff	[44]
Droplet surface tension	N/m	1.77	[45]
Latent heat of solidification	kJ/kg	296	[46]

Table 2.1: Thermophysical properties of nickel in the liquid phase at melting point.

phase model (DPM) is employed for particle tracking with the two-way turbulence coupling method. It is assumed that the volume fraction of particles compared to the continuous phase is negligible, therefore the interaction between particle-particle is not considered. Nickel is uniformly treated as discrete particles, having the same size of melt nozzle, 3.2 mm [47]. The computation is carried out as unsteady simulation with the time step size 10e-6 s. Turbulent dispersion of particles is predicted with the aid of a stochastic tracking model, the Discrete Random Walk that includes the impact of instantaneous turbulent velocity fluctuations on the particle's trajectories [40].

2.2.1 Particle dynamic and droplet breakup

The motion of the particle is simulated by the Lagrangian particle tracking approach. It is assumed that the particles are spherical and inert. The trajectories of the particles are predicted by integrating the force balance equation on the particle within the Lagrangian reference frame. The equation of particle motion is expressed as follows, which equates the particle inertia with the forces acting on the particle

$$m_p \frac{d\vec{u}_{p,i}}{dt} = m_p \frac{(\vec{u} - \vec{u}_p)}{\tau_r} + m_p \frac{\vec{g}\,(\rho_p - \rho)}{\rho_p} + \vec{F} \tag{2.28}$$

where $m_p \frac{(\vec{u}-\vec{u}_p)}{\tau_r}$ and $m_p \frac{\vec{g}(\rho_p-\rho)}{\rho_p}$ are drag and gravitational forces, respectively [40]. The gravitational force term is neglected in this work, since the particle mass is small and its impact on the particle trajectory is negligible. Term $\vec{F}$ denotes additional forces, including thermophoretic and Saffman lift forces in this study. In equation 2.28, m_p, $\vec{u}_p$, and ρ_p are particle mass, velocity, and density, respectively. The parameters $\vec{u}$ and ρ show fluid velocity and density, respectively.

Also, τ_r represents droplet/particle relaxation time which is defined as follows,

$$\tau_r = \frac{\rho_p {d_p}^2}{18\mu} \frac{24}{C_d Re_p} \tag{2.29}$$

where μ is the molecular viscosity of the fluid, d_p represents particle diameter, C_d shows the drag coefficient and Re_p is particle Reynolds number, which is given as below,

$$Re_p = \frac{\rho d_p |\vec{u}_p - \vec{u}|}{\mu} \tag{2.30}$$

Drag coefficient

In equation 2.29, the droplet/particle relaxation time (τ_r) includes the drag coefficient. In this work, the drag coefficient is calculated based on a correlation which considers the effects of particle Reynolds number ($0.2 < Re_p < 10^4$) as well as particle Mach number ($0.1 < Ma_p < 2$) [48]. This range satisfies the particle conditions in the free-fall swirling atomization process. The correlation is proposed by Crowe [48] and expressed as following,

$$C_d = (C_{d(inc)} - 2)e^{-3.07\gamma^{1/2}\left(\frac{Ma_p}{Re_p}\right)g(Re_p)} + \frac{h(Ma_p)}{\gamma^{1/2} Ma_p} e^{\frac{-Re_p}{2Ma_p}} + 2 \tag{2.31}$$

where $C_{d(inc)}$ represents the drag coefficient for a sphere in the incompressible flow which can be obtained from a correlation by Clift et al. [49], and Ma_p, particle Mach number is defined as below,

$$Ma_p = \frac{|u - u_p|}{\sqrt{\gamma R T_g}} \tag{2.32}$$

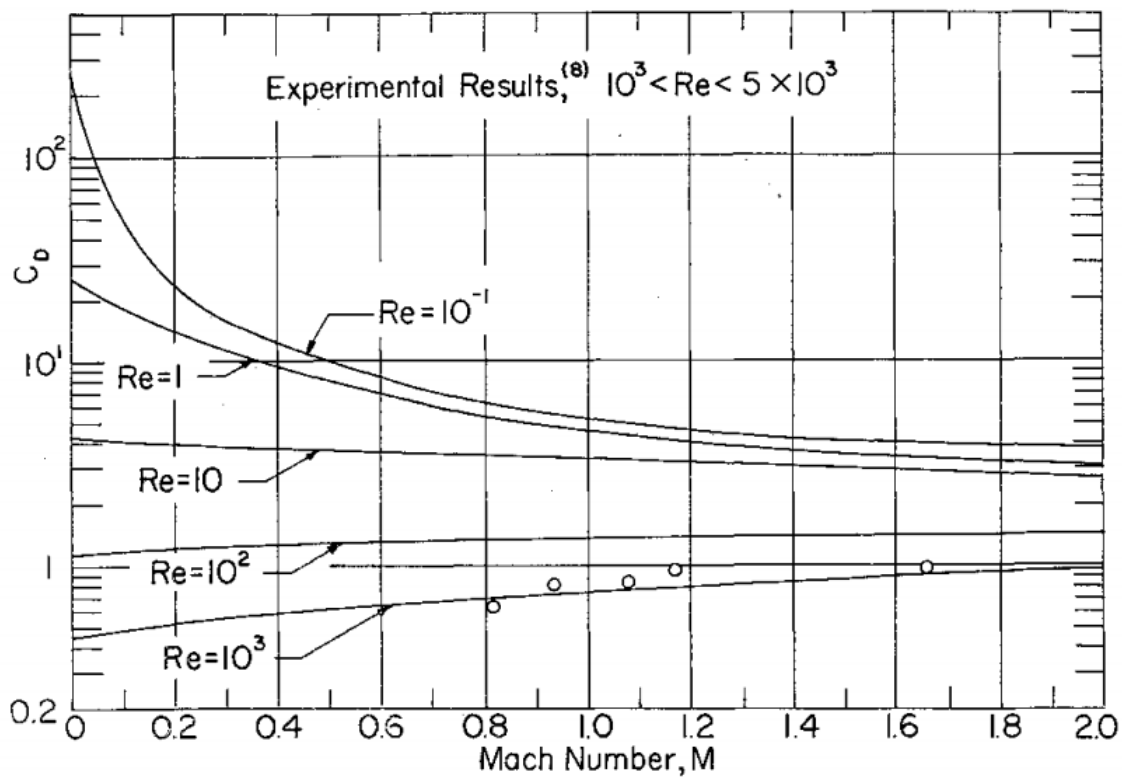

Figure 2.7: Variation of drag coefficient according to the Crowe correlation [48].

Also in equation 2.31, $g(Re_p)$ and $h(Ma_p)$ show the devised functional relations and are written as below, [48]

$$log_{10}g(Re_p) = 1.25[1 + tanh(0.77log_{10}Re_p - 1.92)] \tag{2.33}$$

$$h(Ma_p) = \left[2.3 + 1.7[T_p/T_g]^{1/2}\right] - 2.3tanh(1.17log_{10}Ma_p) \tag{2.34}$$

Figure 2.7 illustrates the variation of the drag coefficient according to the equation 2.31. The correlation was integrated into ANSYS-Fluent's DPM model by a user-defined function (UDF).

Thermophoretic force

During the atomization process, the particles experience a large temperature gradient. Therefore, in the additional force term of equation 2.28, the effect of thermophoretic force is taken into consideration. Thermophoretic force is exerted on the particles in the direction opposite to that of the temperature gradient and written as below [44],

$$\vec{F} = -D_{T,p}\frac{1}{T}\nabla T \tag{2.35}$$

where *T* is local fluid temperature and $D_{T,p}$ represents thermophoretic coefficient which is proposed by Talbot [44] and defined as following,

$$D_{T,p} = \frac{6\pi d_p \mu^2 C_s (K + C_t Kn)}{\rho(1 + 3C_m Kn)(1 + 2K + 2C_t Kn)} \tag{2.36}$$

here *Kn* is Knudsen number and *K* is defined as k/k_p where *k* is the fluid thermal conductivity based on the translational energy only ($(15/4)\mu R$) and k_p is the particle thermal conductivity. Also, the constants C_s, C_t, and C_m are 1.17, 2.18, and 1.14, respectively. This expression is based on the assumption of spherical particles and ideal gas [40].

Saffman lift force

Saffman lift force is also considered for the additional force term of equation 2.28 and defined as following,

$$\vec{F} = m_p \frac{2K\nu^{1/2}\rho d_{ij}}{\rho_p d_p (d_{lk} d_{kl})^{1/4}} (\vec{u} - \vec{u_p}) \tag{2.37}$$

where k=2.594 and d_{ij} denotes the deformation tensor [50]. During the free-fall swirling atomization process, there is a large relative velocity between the particles and gas flow which can affect the Saffman lift force, as shown in equation 2.37. This form of the lift force is used for the small particle Reynolds numbers [40].

Droplet breakup model

The breakup phenomenon is a complicated, multi-factor process. As the complex interaction between two phases takes place in a fraction of second, studying the breakup phenomenon is challenging [51]. To determine the type of secondary breakup mechanism, dimensionless Weber number parameter is used [18], defined as,

$$We = \frac{\rho_g U_{rel}^2 d_p}{\sigma} \tag{2.38}$$

where ρ_g, U_{rel}, d_p, and σ are the gas density, relative velocity of gas with respect to the droplet, particle/droplet diameter, and surface tension of the molten metal droplet, respectively. It should be noticed that the assumption of constant surface tension of the liquid phase is made during the entire disintegration process, as represented in table 2.1. Figure 2.8 illustrates the classification of breakup mechanism based on the Weber number which is done by Pilch and Erdman [52]. According to this classification, when the Weber number is smaller than 12, the breakup phenomenon does not take place and the droplets are just deformed. For the Weber number greater than 12, the classification represents as follows

$12 \leq We \leq 100 \Longrightarrow$ Bag breakup

$100 \leq We \leq 350 \Longrightarrow$ Stripping breakup

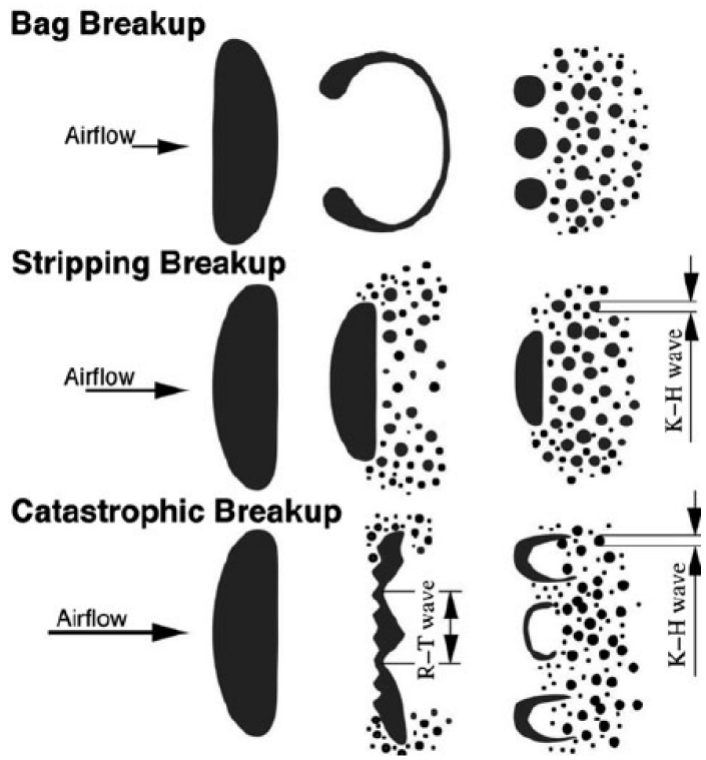

Figure 2.8: Breakup regimes based on Weber number [53].

$We \geq 350 \Longrightarrow$ Catastrophic breakup

Considering the above classification, as the Weber number at any point of the focal area is larger than 100, the Kelvin-Helmholtz Rayleigh-Taylor (KHRT) breakup model is applied. This model is well suited for the high Weber numbers, greater than 100, and catastrophic breakup. In the atomization process, the focal zone is the place that the catastrophic breakup of melt droplets occurs. The KHRT breakup mechanism combines the effects of Kelvin-Helmholtz waves driven by aerodynamic forces and Rayleigh-Taylor instabilities originated from the acceleration of shed droplets ejected to the gas flow [40, 54].

In the KHRT breakup model, it is assumed that there is a liquid core in the near nozzle region and the droplets are shed from this liquid core, as shown in Fig. 2.9. Inside the liquid core region, only the effects of Kelvin-Helmholtz waves driven by aerodynamic forces are considerable and

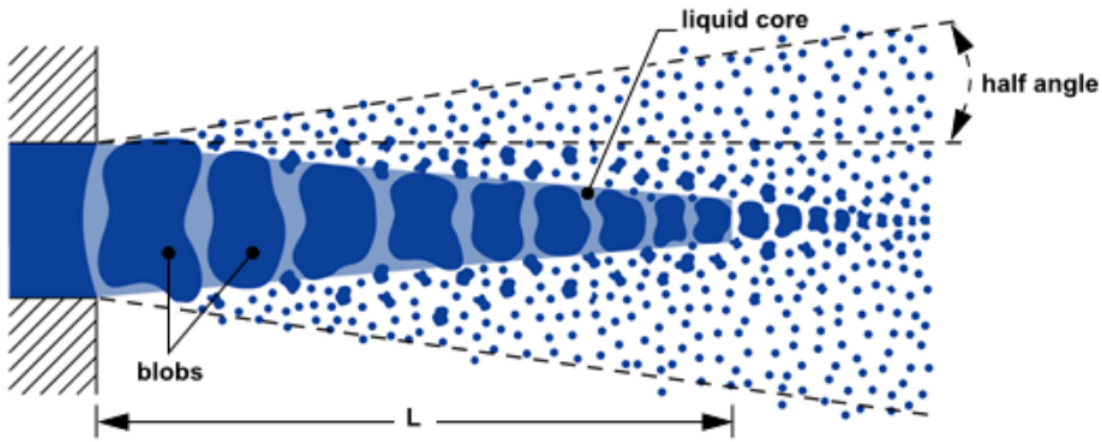

Figure 2.9: Liquid core approximation [40].

dominant. When the liquid core diminishes and the droplets reach the freestream, they start to get accelerated and the effects of Rayleigh-Taylor instabilities become dominant. The length of this core is calculated from Levich theory as below [40],

$$L = C_L d_0 \sqrt{\frac{\rho_l}{\rho_g}} \tag{2.39}$$

where C_L and d_0 are the Levich constant and reference nozzle diameter, respectively. The details of droplet breakup are explained as below.

In the wave breakup model, the relative velocity between the injected droplets and the gas flow results in the aerodynamic instabilities. The radius of the newly formed droplets can be computed based on the wavelength of the fastest-growing unstable surface wave on the parent droplet [40], defined as below,

$$r = B_0 \Lambda \tag{2.40}$$

where B_0 is the model constant (=0.61). The rate of the droplet radius is calculated from

$$\frac{da}{dt} = -\frac{(a-r)}{\tau} \qquad r \leq a \tag{2.41}$$

where τ, breakup time is calculated from

$$\tau = \frac{3.726 B_1 a}{\Lambda \Omega} \tag{2.42}$$

and B_1 is the breakup time constant and equal to 1.73. The parameters of Λ and Ω are given as following,

$$\frac{\Lambda}{a} = 9.02 \frac{(1+0.45Oh^{0.5})(1+0.4Ta^{0.7})}{(1+0.87We_2^{1.67})^{0.6}} \tag{2.43}$$

$$\Omega \sqrt{\frac{\rho_1 a^3}{\sigma}} = \frac{0.34 + 0.38We_2^{1.5}}{(1+OH)+(1+1.4Ta^{0.6})} \tag{2.44}$$

where $Oh = \sqrt{We_1}/Re_1$ is the Ohnesorge number and $Ta = Oh\sqrt{We_2}$ is the Taylor number. Moreover, We_1 and We_2 represent the liquid and gas Weber numbers, respectively and Re_1 is the Reynolds number and equal to $U\frac{a}{\nu_1}$, where a is the liquid jet radius and ν_1 is the dynamic viscosity of liquid [40].

A new parcel is created when the shed mass reaches 5% of the initial mass. The radius of newly formed droplets could be computed from equation 2.40. The new parcel would be the same as their parent parcels in some properties like position, temperature, material and so forth except for the velocity and radius [40].

Rayleigh-Taylor breakup

Similar to Kelvin-Helmholtz (KH) model, the Rayleigh-Taylor (RT) breakup model describes wave instabilities formed on the droplet surface. The frequency of the fastest growing wave is calculated by

$$\Omega_{RT} = \sqrt{\frac{2(-g_t(\rho_p - \rho_g))^{3/2}}{3\sqrt{3\sigma}(\rho_p + \rho_g)}} \tag{2.45}$$

where g_t denotes the acceleration of droplet in the direction of droplet motion [40]. The corresponding wave number is computed from

$$K_{RT} = \sqrt{\frac{-g_t(\rho_p - \rho_g)}{3\sigma}} \tag{2.46}$$

After the Rayleigh-Taylor waves grow for a time greater than the breakup time (τ_{RT}), the droplet breakup takes place. The breakup time is written as below,

$$\tau_{Rt} = \frac{C_\tau}{\Omega_{RT}} \tag{2.47}$$

where C_τ represents the Rayleigh-Taylor breakup time constant and has the default value of 0.5 [40].

The wave growth can be tracked until the predicted wave length $\frac{2\pi C_{RT}}{K_{RT}}$ reaches lower than the local droplet diameter. The radius of smaller child droplets is obtained from

$$r_c = \frac{\pi C_{RT}}{K_{RT}} \tag{2.48}$$

here C_{RT} is the breakup radius constant. The default value for C_{RT} is equal to 0.1 [40].

2.2.2 Particle heat transfer

To simulate the particle heat transfer, the Lumped capacity method is utilized as the particle Biot number is smaller than 0.1. The solver, ANSYS-Fluent employs a simple heat balance equation to make a relation between the particle temperature (T_p) and the convective heat transfer. The heat balance equation is expressed as below,

$$m_p c_p \frac{dT_p}{dt} = hA_p(T_\infty - T_p) \tag{2.49}$$

where m_p, c_p, and A_p are mass (kg), heat capacity (J/kg K), and surface area (m^2) of the particle, respectively. Also, T_∞ represents local temperature of the continuous phase (K) and *h* denotes convective heat transfer coefficient (W/m^{2}K). In equation 2.49, it is assumed that there is no internal temperature gradient within the particle, meaning the particle temperature is uniform throughout [40]. For this investigation, the convective heat transfer coefficient is customized and the effects of latent heat of solidification and shrinkage factor are taken into account. All these considerations are explained in detail as follows.

2.2.2.1 Nusselt number model

The heat transfer coefficient is calculated from the Nusselt number (*Nu*), the thermal conductivity of the gas (K_g), and the particle diameter (d_p), as shown below,

$$h = \frac{NuK_g}{d_p} \tag{2.50}$$

The solver is used Ranz-Marshal correlation for the calculation of Nusselt number. But,

in this work, the Nusselt number is customized by using Kavanau correlation rather than the Ranz-Marshall correlation in order to include the impacts of rarefaction and high Mach number [55, 56]. The code is implemented into the solver by the user-defined function (UDF). The Nusselt number of Kavanau correlation is given as follows,

$$Nu = \frac{Nu_0}{1 + 3.42 Nu_0 \frac{Ma}{Re_p Pr}} \tag{2.51}$$

where *Ma* is the Mach number and Nu_0 is the Nusselt number obtained from the Ranz-Marshall correlation and written as below [40],

$$Nu_0 = 2 + 0.6 Re_p^{1/2} Pr^{1/3} \tag{2.52}$$

here Re_p is the Reynolds number based on the particle diameter and the relative velocity, as shown in equation 2.30, and *Pr* is Prandtl number which is defined as following,

$$Pr = \frac{c_p \mu}{k_g} \tag{2.53}$$

where μ is the dynamic viscosity of the continuous phase [40].

2.2.2.2 Latent heat of solidification

Jabbari et al. developed a computationally inexpensive approach to model the melting phenomenon [46]. This method is utilized for modeling the latent heat of solidification of particles during phase change, in which the impact of huge amount of released energy over phase change is simply taken into consideration. The particle temperature profile is implemented into the

solver using a piece-wise linear function which is defined as Fig. 2.10. As the phase change happens from liquid to solid, the specific heat of pure nickel in the liquid and solid phases are applied to temperatures greater than the melting point and lower than 1718 K, respectively. The latent heat of solidification is approximated as below [46],

$$C\Delta T = H \tag{2.54}$$

where H is the heat of solidification, ΔT is assumed to be 10 K (from 1728 to 1718 K), and C is the estimated specific heat which is around 29.6 kJ/kg. This approach is successfully verified for modeling the latent heat over phase change of single [57] and multi-component [58,59] droplets.

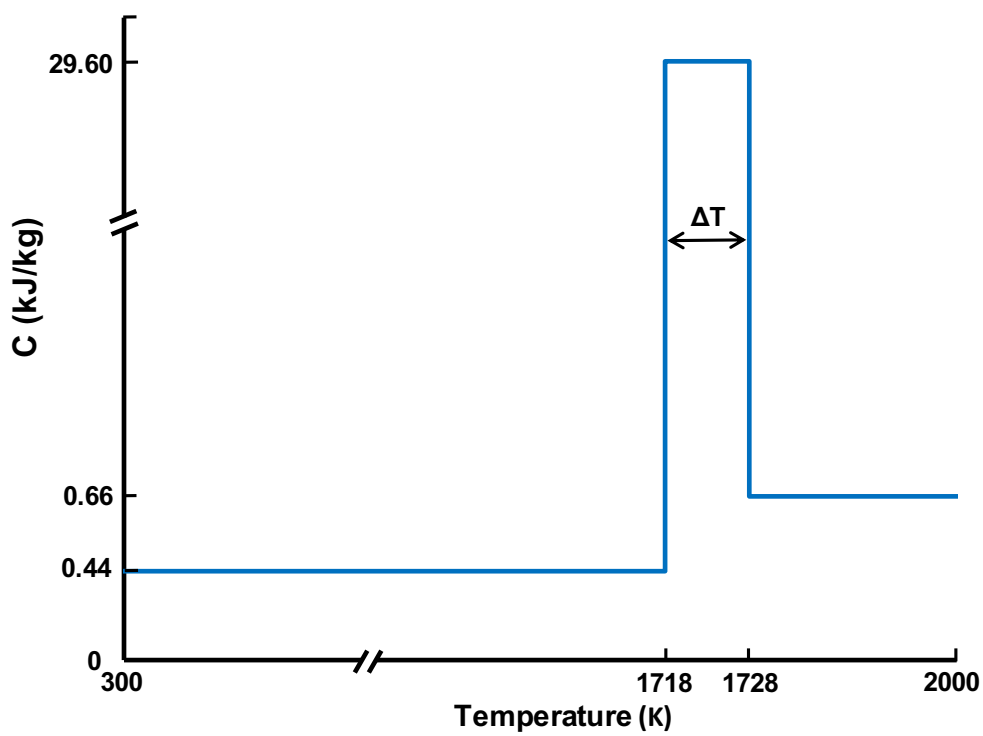

Figure 2.10: Variation of specific heat of dispersed phase as a function of temperature.

2.2.2.3 Shrinkage coefficient

The density of nickel is inversely proportional to the temperature [60]. During the atomization process, the particle temperature drops dramatically due to the solidification and cooling, while the particle density rises steadily. This temperature drop leads to the occurrence of shrinkage phenomenon since the volume decreases with the increase in density [61]. As the particles are assumed to be spherical and the particle mass stays constant, the resulting particle size distribution can be affected by the variation of density. For the sake of including this effect on the particle size distribution, the following calculation is made

$$\frac{d_{p,s}}{d_{p,l}} = \sqrt[3]{\frac{\rho_l}{\rho_s}} \tag{2.55}$$

where $d_{p,s}$ and $d_{p,l}$ are the particle/droplet diameter of solid phase at room temperature and liquid phase at melting point, respectively. Parameters ρ_s and ρ_l denote the particle density of solid and liquid phases in the corresponding temperatures, respectively. Subsequently, the particle size distribution of nickel falls around 5% during the entire atomization process, leading to more accurate results. This coefficient is applied to the resulting PSD from the solver throughout this study.

Chapter 3

Results and discussion

Overview

In this chapter, numerical results for the continuous and dispersed phases are presented including the baseline case. Moreover, the effects of changing process parameters such as gas-to-melt ratio, number of nozzles, and parent droplet size are discussed. In the end, the impacts of changing the design factors like radial and swirl angles are presented.

This work carries out a numerical, parametric study on the free-fall swirling gas atomizer using the discrete phase model. It aims at providing practical techniques and guidelines to narrow down the particle size distribution and reduce the particle median diameter. To do so, in the first step, a baseline case is analyzed in both continuous and dispersed phases, then, some of the process parameters are compared in a range of gas-to-melt ratios, number of gas nozzles and parent droplet size. Finally, the effect of change in radial and swirl angles are investigated.

3.1 Baseline case

Figure 3.1 shows an overview of the atomization process for the baseline case using iso-surfaces of gas velocity magnitude. A 6-nozzle free-fall swirling configuration with the inclusion of 11-cm sleeve is considered for the baseline model. The radial (α) and swirl (β) angles (as shown in Fig. 1.7) are also set at 10° and 5°, respectively. It should be noticed that the computational domain, methods, and assumptions are the same as stated in the methodology chapter.

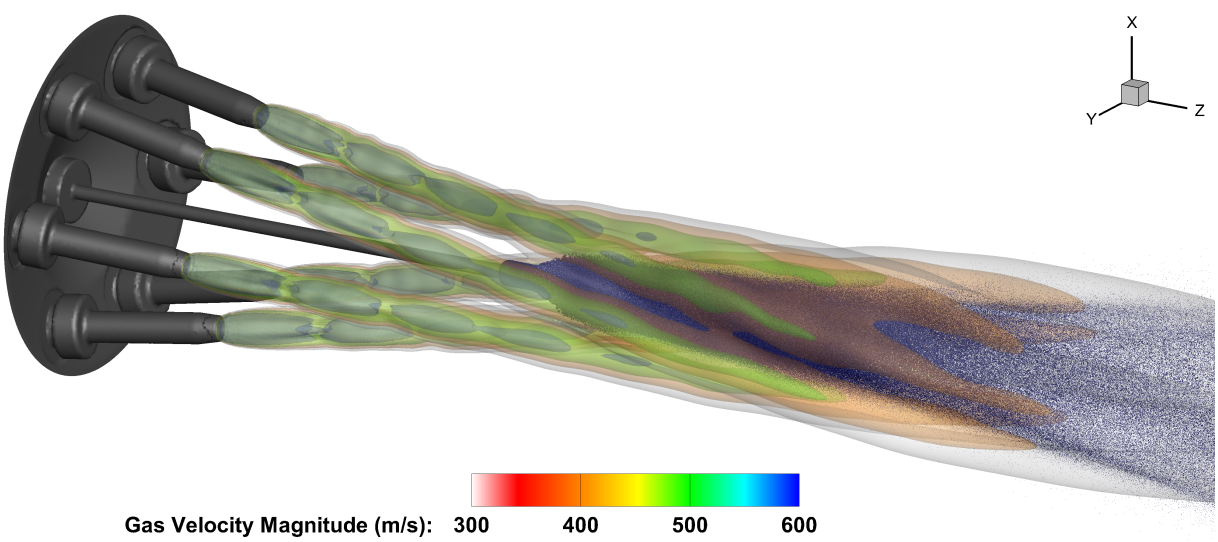

Figure 3.1: Iso-surface of gas velocity magnitude for the baseline case.

3.1.1 Continuous phase

The nitrogen gas flows through the de Laval nozzles, featuring a throat diameter of 3 mm, with the mass flow rate of 4.67 kg/min (i.e. 28 kg/min for the 6 nozzles in total). The compressible gas is injected under high operating pressure. This condition leads to developing supersonic under-expanded jet in the exhaust stream. In other words, since the ambient pressure is lower than the pressure of nozzle exit, the compressed flow is expanded by Prandtl-Meyer expansion fans, followed by normal and oblique shock waves. Shock diamond patterns can be simply formed by a pair of oblique shock and expansion fans [62]. The existing wave structures in the exhaust stream are strong enough to create at least 5 shock diamond patterns and hit the Mach number of 5 as illustrated in Fig. 2.6. The whole shock diamond patterns are clearly displayed in Fig. 3.2 with the aid of static pressure and gas velocity contours for the nozzle cut plane placed parallel to the gas stream. The static pressure and gas velocity magnitude could reach over 5 MPa and 700 m/s, respectively. It should be indicated that the contour level of static gauge pressure variable is omitted for the values above 800 kPa for the sake of a better representation of shock structures.

3.1.2 Dispersed phase

Figure 3.3 displays the interaction of gas flow and molten metal stream during the development of gas velocity field in the z-direction, i.e. along the melt discharge direction. The gas velocity field presented at normal planes apart 4 cm from each other, shows that how the particles get surrounded by the high-speed gas flows. It is observed that the particle trajectories begin to deviate from the centerline after the gas velocity magnitude reaches roughly 400 m/s. This deviation

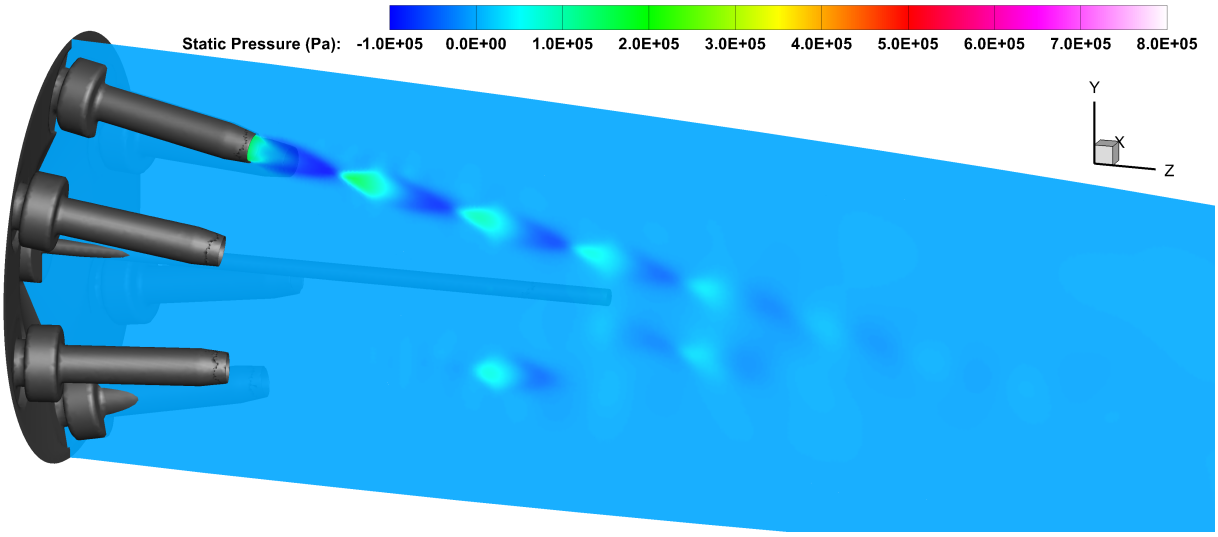

(a)

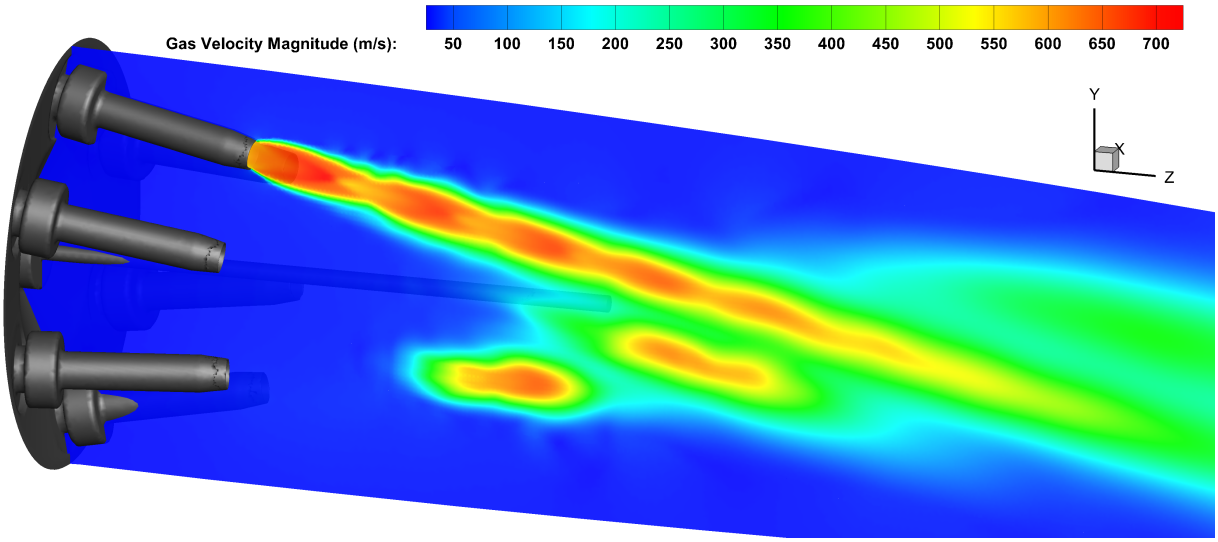

(b)

Figure 3.2: An illustration of shock diamond patterns over the contour of (a) static pressure and (b) gas velocity magnitude.

can be seen in Fig. 3.1 as well. The reason for this behavior is the gas radial momentum as well as further secondary breakups. Through axial direction, the progress of secondary breakup forms smaller particles that follow the gas stream. In the baseline arrangement, the melt stream is introduced to 6 high-velocity gas jets with the help of sleeve at z=11 cm and starts to get

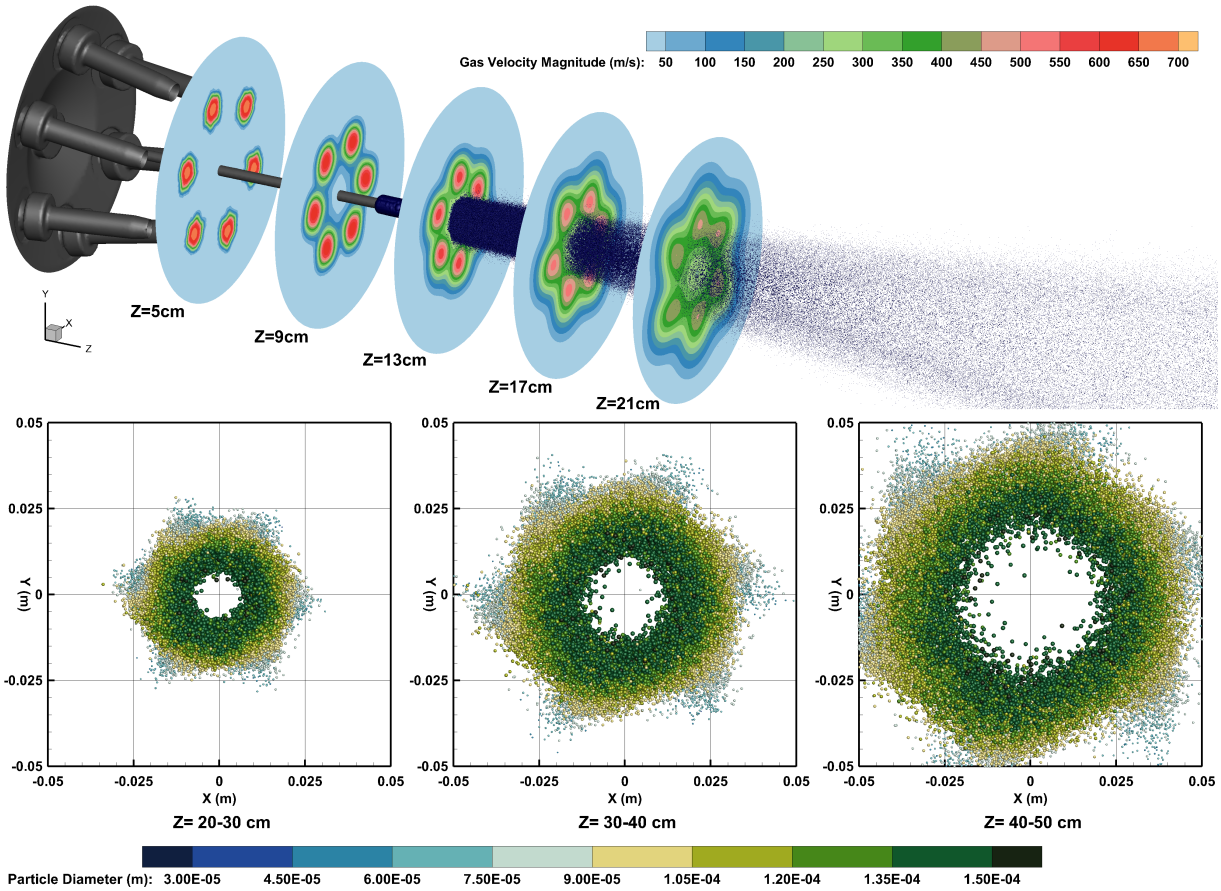

Figure 3.3: Baseline case: interaction between the gas flow and melt stream with the footprint of in-flight particles at different stand-off distances.

disintegrated over the range of z=12-13 cm.

Figure 3.3 also shows the footprint of in-flight particles lying in the size range below 150 μm through three successive stand-off distances. Those particles which have the sizes above 150 μm, are concentrated in the centerline of domain and eliminated from the particle footprints only due to the better representation of smaller particles distribution. Figure 3.3 reveals that the larger particles can be mostly found around the centerline of entire domain, whilst the smaller ones travel far away from the domain core owing to the existing supersonic gas jets. In fact, the smaller particles are literally produced somewhere adjacent to the core of gas jets containing higher kinetic energy and momentum. It proves that the particle size is heavily dependent

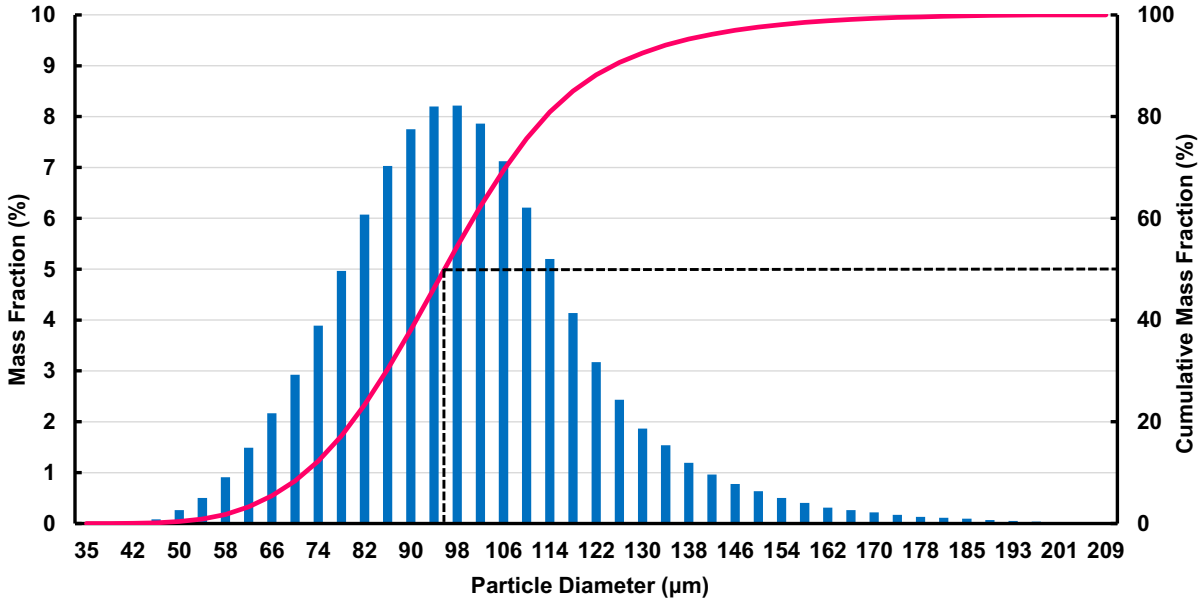

Figure 3.4: PSD and cumulative particle size distribution of the baseline case.

on the gas momentum which is observed in other investigations as well [21, 33]. In order to quantitatively explore and compare the resulting PSD and d_{50} of different scenarios with the baseline case, samples are taken and sorted from the droplets at the downstream of domain, that is axial distance of 50 cm. Figure 3.4 illustrates the unimodal volume distribution of particles for the baseline model, ranging from 35 to 210 μm and reporting mass median diameter of approximately 95 μm.

3.2 Gas-to-melt ratio effect

In the present work, gas-to-melt mass flow rate ratio (GMR), also known as mass loading ratio [24], is defined as the ratio of the continuous-phase mass flow rate (i.e. mass flow rate of all gas nozzles) to the dispersed-phase mass flow rate. This ratio is the key parameter to control the mass median diameter and particle size [15, 39]. To view the influence of GMR on the resulting

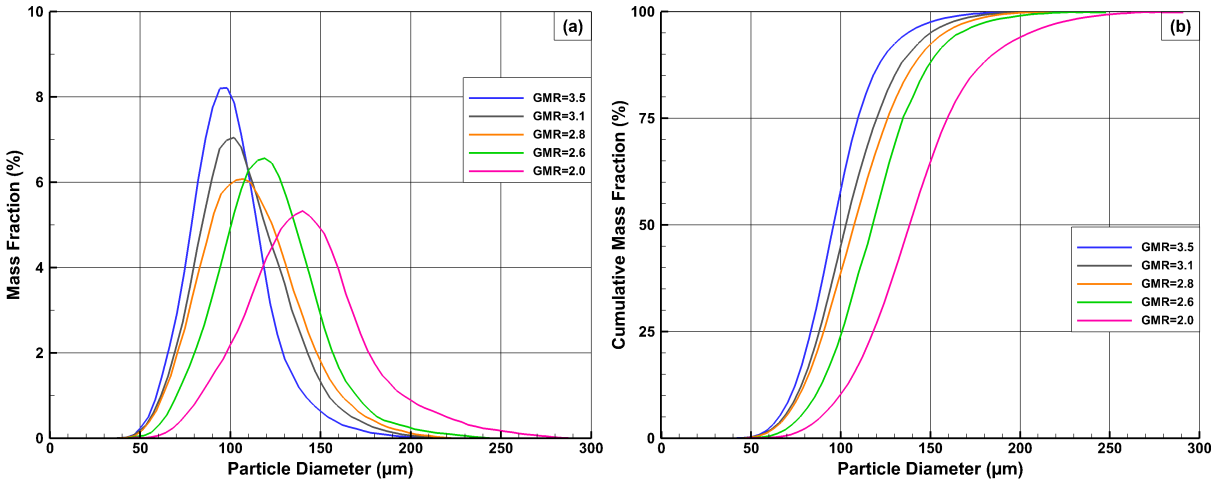

Figure 3.5: Impact of change in gas-to-melt mass flow rate ratio on the PSD and cumulative particle size distribution for the baseline case.

d_{50} and PSD, two variables, back pressure (which is nitrogen back pressure in the nozzles) and melt mass flow rate are studied, as represented in Fig. 3.5. The back pressure is plotted for the values of 5 (GMR=3.5), 4 (GMR=2.6), and 3 MPa (GMR=2.0) with the identical melt mass flow rate. Fundamentally, altering the back pressure changes the gas mass flow rate at each gas inlet, which results in the change in the delivered gas velocity to the atomization zone. The numerical results indicate that decreasing the back pressure from 5 (baseline case) to 3 MPa not only shifts the peak of PSD towards larger particle size, but also declines the mass percentage of the peak of PSD dramatically, which is attributed to a wider particle size distribution ultimately. The main reason for this behavior is the reduction of relative velocity which causes a fall in the Weber number and affecting the progress of breakup. Under these three different GMR conditions for the back pressure, that is from GMR=3.5 to GMR=2.0, the mass median diameter can be noticeably varied between 95 and 135 μm.

As illustrated in Fig. 3.5, this trend can also be observed for the other parameter, i.e. melt mass flow rate, for the values of 8, 9, and 10 kg/min, resulting in GMRs of 3.5, 3.1, and 2.8,

respectively. As it can be seen, the increase in melt mass flow rate could make the mass median diameter larger, from 95 to 110 μm. Through this comparison, since the gas mass flow rate is kept fixed, the delivered gas velocity to the atomization area remains unchanged; whereas, the melt mass flow rate rises from 8 (baseline case) to 10 kg/min, which contributes to a negligible increase in velocity of parent particles. The variations of PSD and d_{50} for melt mass flow rate report that under the same continuous-phase operating condition, the thicker the melt stream is, the greater the size of melt drop is produced by the atomization process. It can be concluded that the increase in GMR for both variables results in the formation of smaller droplets, which is favorable for this work.

3.3 Number of nozzles effect

In Fig. 3.6, the gas velocity field of the case of 4-nozzle die is compared with the cases of 6-nozzle (i.e. baseline) and 8-nozzle die for the same static pressure of 5 MPa at the inlet of gas nozzles. To examine the effect of number of nozzles, the back pressure of each nozzle needs to be constant. Therefore, the amount of mass flow rate at the inlet plane of each nozzle, remains unchanged in each scenario. Practically, the back pressure of the gas nozzles is provided by a large plenum chamber to avoid any sort of pressure drop during the atomization process. In comparison between 8-nozzle and 4-nozzle cases, if each gas jet is considered as an attack point, the melt stream gets much more disintegrated in 8-nozzle layout which literally means 8 attack points.

Figure 3.7 shows the influence of the number of nozzles on PSD and cumulative particle size distribution for the inlet static pressures of 3 and 5 MPa. Both graphs confirm that the size

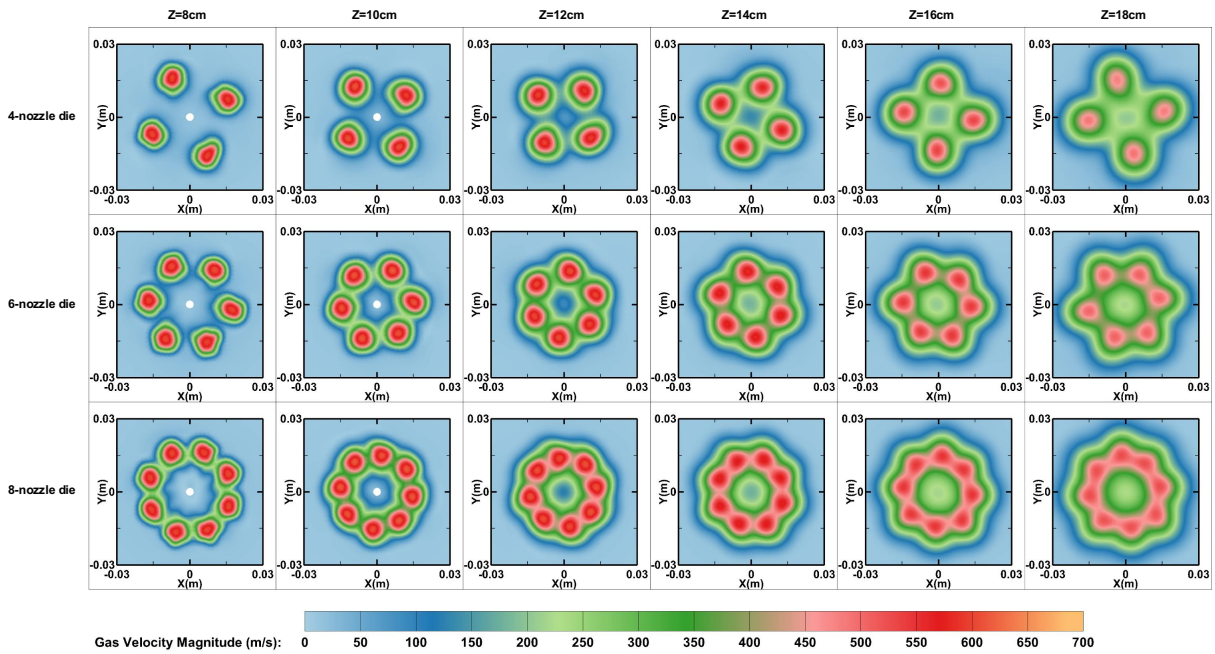

Figure 3.6: The gas velocity field of 4-nozzle, 6-nozzle and 8-nozzle die at various stand-off distances for P_{back}=5 MPa.

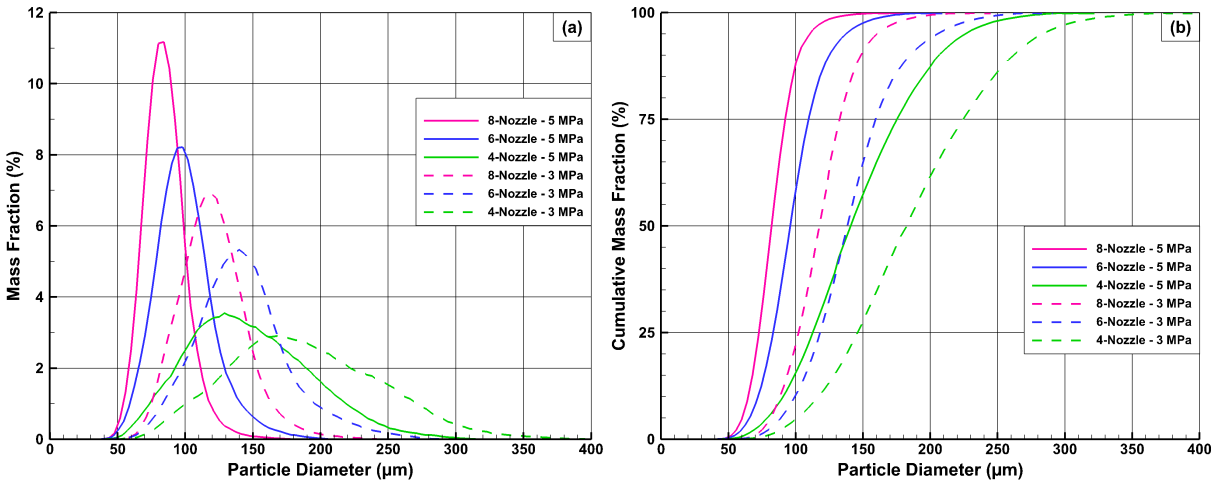

Figure 3.7: Effect of the number of nozzles on the PSD and cumulative particle size distribution for the pressures of 3 and 5 MPa at the gas nozzle inlet.

distribution obtained from 8-nozzle arrangement could remarkably narrow down the resulting PSD and improve the d_{50} up to approximately 35-40% in comparison with the case of 4-nozzle die. The reason for this notable improvement is that using higher number of nozzles results

in more impact area of high-velocity gas stream on the molten liquid at the impingement zone and causes more intensive fragmentation of the particles. Furthermore, Fig. 3.7 proves that the higher inlet pressure could produce smaller particles owing to more momentum flow rate, as stated in the previous section. It should be mentioned that the back pressure of 5 MPa with 6 gas nozzles is considered as the baseline case.

3.4 Effect of parent droplet size

The Weber number is of importance in the simulation of atomization process and determines the regime of breakup [17]. Since this factor is proportional to the droplet diameter, the parent droplet size is considered to be examined for the sizes 3.2 (baseline case), 4.2, and 5.2 mm, as shown in Fig. 3.8. It was observed that varying the initial droplet diameter (i.e. molten metal jet diameter) results in a similar trend for the PSD and d_{50} to those of the baseline case. This behavior originates from high relative velocity of gas with respect to droplets. As a matter of

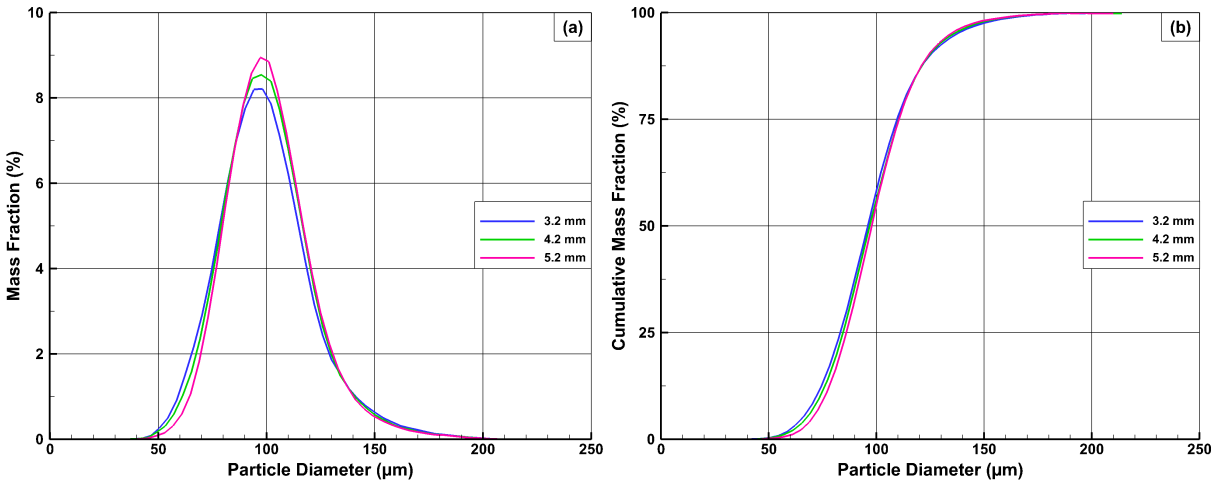

Figure 3.8: Impact of change in the parent droplet size on the PSD and cumulative particle size distribution of 6-nozzle die under the same operating condition.

fact, the change in parent drop size in the order of millimeter does not contribute to the change in the breakup regime of droplets and the value of Weber number changes negligibly. It can be concluded that the relative velocity dominates throughout the disintegration process and the Weber number substantially depends upon the relative velocity rather than parent drop size.

3.5 Effect of radial angle

In the previous sections, the effects of process parameters are accounted for in various scenarios, while sections 3.5 and 3.6 are aimed at studying the influence of design factors, that is radial and swirl angles. Through the following configurations, since the droplets are introduced to the gas jets at different stand-off distances, the sleeve feature is eliminated from the baseline case. It makes a slight difference in the PSD and d_{50} that can be observed in the following results.

Throughout this work, the radial angle is denoted as α and analyzed over the range of 8° to 14° with the same swirl angle, 5° under the same continuous- and dispersed-phase conditions as the baseline case. Figure 3.9 illustrates an overview of how the flow field is developed for various radial angles using three different iso-surfaces of gas velocity magnitude. The swirl motion of gas streams along axial direction leaves some space between the gas jets, as shown in Fig. 3.9. This space is called ”leftover room” in this study. Figure 3.9 shows that the leftover room between the gas jets at the same gas velocity iso-surface diminishes with increasing the radial angle. In the free-fall swirling configuration, optimizing this space could improve the controllability of atomization process to a great extent. Indeed, the leftover room should not be that tight since it raises the chance of melt build-up on the gas nozzle tip and the melt stream might be even clogged in the melt delivery tube. On the other hand, widening the leftover room

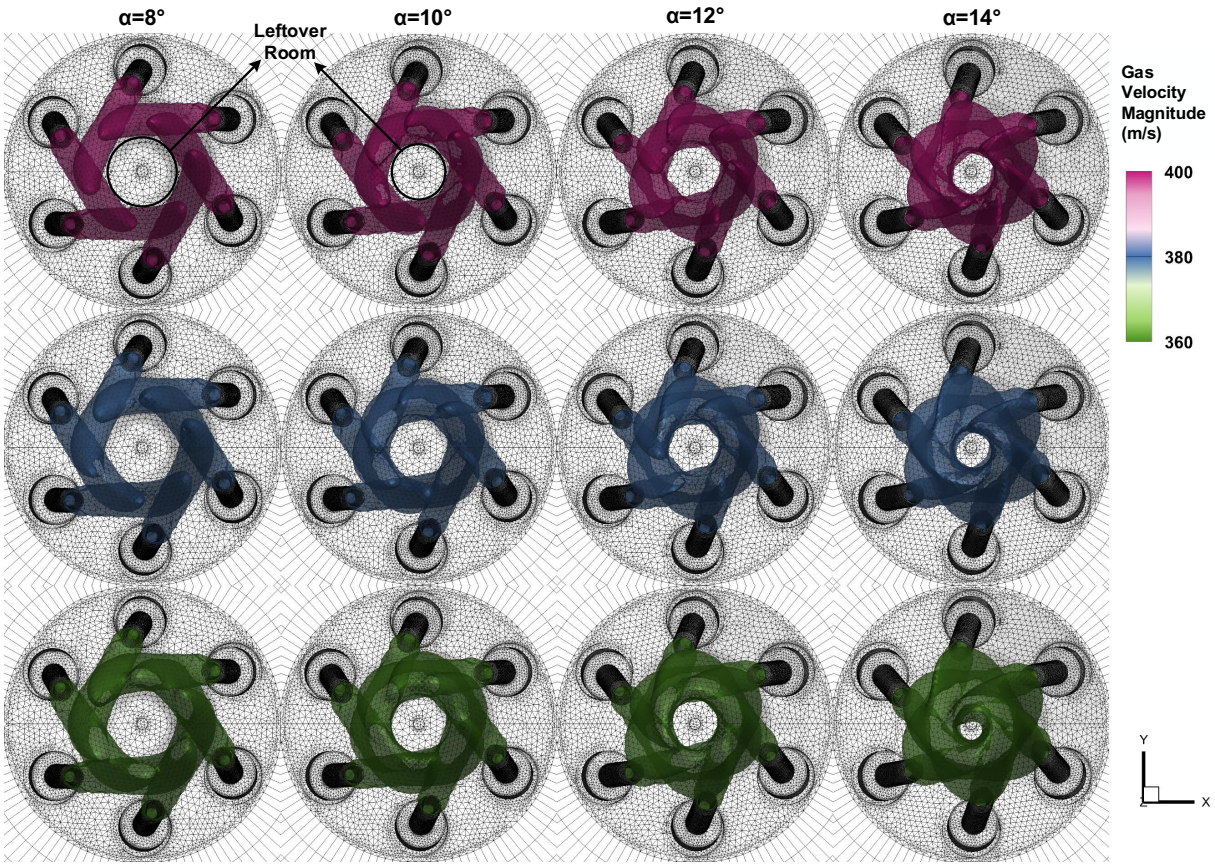

Figure 3.9: Front view of gas velocity iso-surfaces for different radial angles with the same tangential angle of 5°.

may bring about exposing the melt stream to low-velocity gas flow field and wasting the kinetic energy of the gas jets. As a result, this critical space should be controlled and balanced perfectly in order to benefit the most from the available gas momentum.

The streamline distribution of continuous phase is shown in Fig. 3.10 for cases α=10° (baseline) and 14°. Figure 3.10 simply clarifies the swirl motion of gas flow around the melt stream and how the gas jet disrupts the molten metal stream into a shower of droplets around the focal point of disintegration zone. In the case of α=14°, it is obvious that the liquid and gas phases meet each other at a closer point to the melt exit due to the steeper attack angle, showing that increasing the radial angle from 10° to 14° leads the focal point to be transferred from around

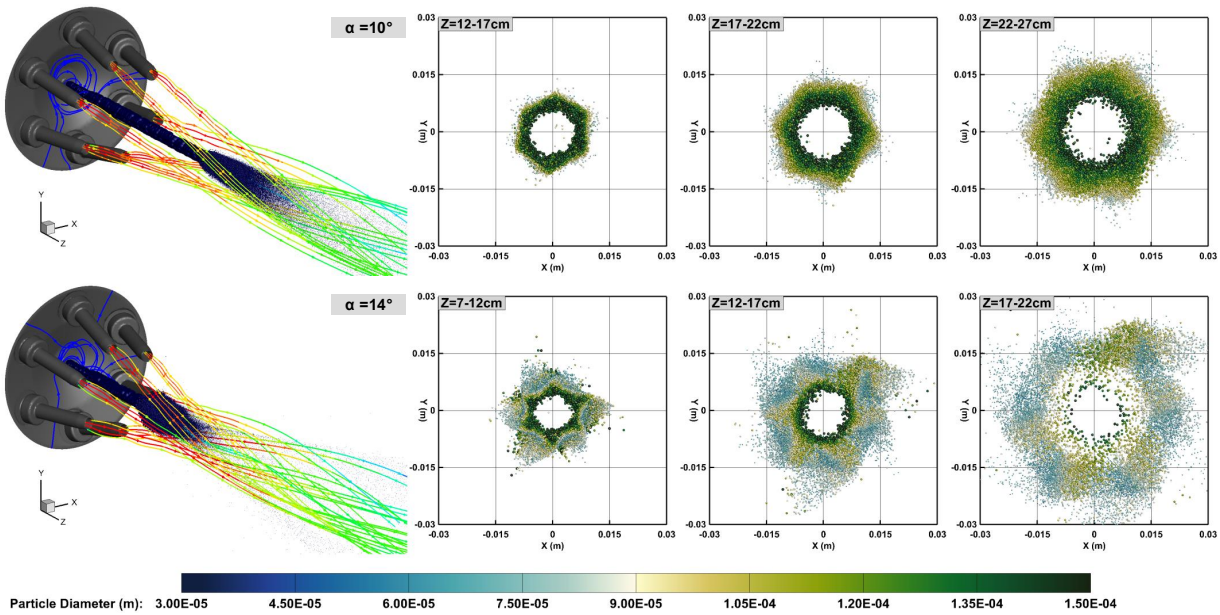

Figure 3.10: Streamlines of gas flow for α=10° (baseline case) and α=14° with the footprint of in-flight particles over various stand-off distances downstream the focal point.

12 to 7 cm and causes more intensive disintegration of droplets. After the focal point, the fine particles follow the gas streamlines owing to the high relative velocity. Moreover, it should be noticed that placing the focal point so much close to the gas jets could raise the chance of melt build-up and clogging the nozzles, which contributes to failure in proceeding the atomization process. As a result, increasing the radial angle could be practical up to a certain extent.

Figure 3.10 also displays the footprint of in-flight particles for the cases of α=10° and 14° for three consecutive 5-cm stand-off distances downstream the focal point. The particle diameter above 150 μm is omitted from these plots due to a better representation of particle size distribution. Both cases confirm that the more the particles travel through the axial direction, the more the particles undergo the breakup process. The larger particles are mainly spotted in the domain core, while, the smaller ones are mostly found somewhere close to the core of gas jets, as explained in section 3.1.2 as well. In the case of α=14°, owing to the occurrence of

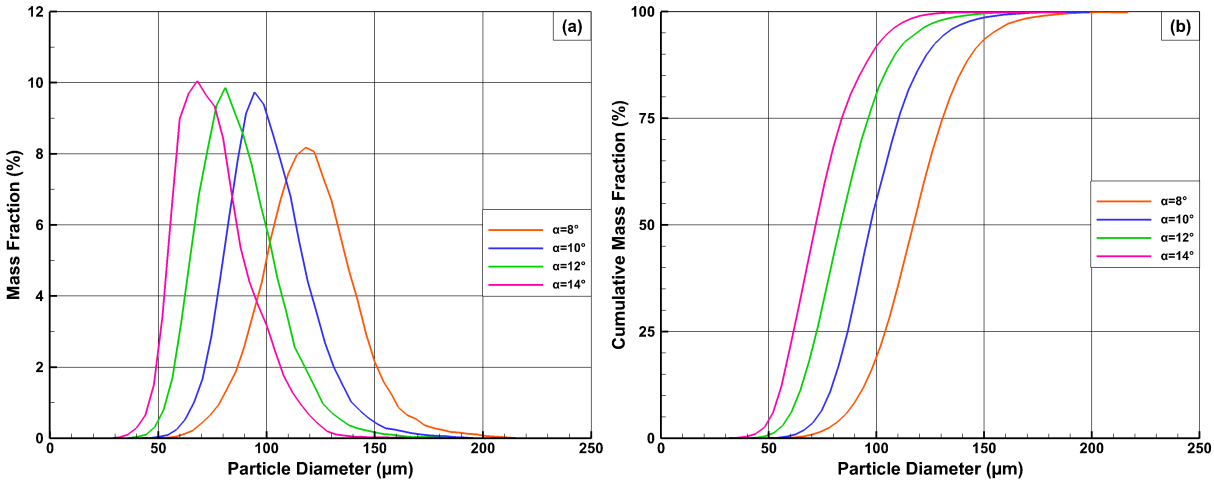

Figure 3.11: Effect of change in the radial angle on the PSD and cumulative particle size distribution of 6-nozzle die under the same operating condition.

more intensive breakup at the focal point, the particles are much more disintegrated at the same stand-off distances downstream the focal point, compared to the case of α=10°.

For the sake of a quantitative assessment of radial angle study, the PSD and cumulative particle size distribution of cases, from α=8° to 14°, are compared and plotted in Fig. 3.11. Increasing the radial angle makes the PSD greatly narrower and shifts it to the left, meaning that not only the peak of the graph stands on the smaller particle diameter, but also it gives a rise to the mass fraction. The effect of this trend appears on the resulting d_{50} in such a way that the mass median diameter drops roughly 40%. The main reason behind this huge decrease is that the parent droplets are impinged by larger gas kinetic energy and momentum flow rate at steeper radial angles.

3.6 Effect of swirl angle

According to the analysis of section 3.5, the narrowest PSD and smallest d_{50} are obtained from the radial angle of 14°. Therefore, this radial angle is selected to examine the effect of swirl

angle variations. The swirl angle is denoted as β and ranges from $4°$ to $7°$. It should be noted that all scenarios are performed under the same operating condition with the exclusion of the sleeve and compared with the case of α=$14°$ and β=$5°$, which is taken from the radial angle study section.

Figure 3.12 is a representation of gas velocity fields over various swirl angles with the same radial angle of $14°$. As it can be seen, the leftover room between the gas jets rises with the increase in swirl angle which is not advisable, since this deviation of gas nozzles causes a huge reduction in the impact area of gas momentum on the parent drops. When the radial angle is optimized for the most effective practical attack angle, a small change in the swirl angle could

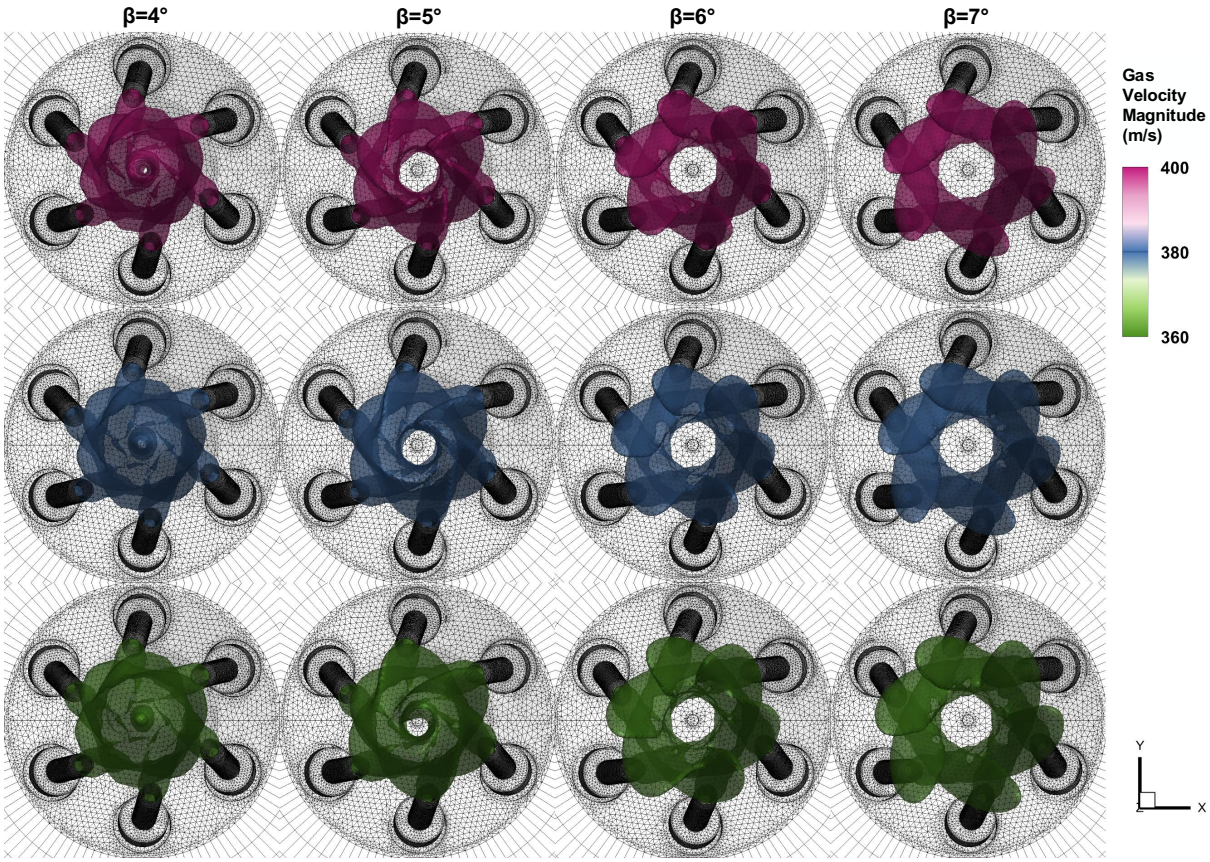

Figure 3.12: Front view of gas velocity iso-surfaces for different swirl angles with the same radial angle of $14°$.

lead to a considerable change in the results. Owing to this sensitivity, the swirl angle range is split into the difference of $1°$, unlike the radial angle. For the case of β=$4°$, the leftover room between the gas jets is completely faded through all three velocity iso-surfaces, i.e. the melt droplets might struggle to pass by the focal point and could splash back to the die body. Thus, the case of β=$4°$ might be functionally problematic. Raising the swirl angle to 5° can make a huge difference in the results compared to the case of β=$4°$. The case of β=$5°$ not only could provide quite enough room between the gas jets, but also facilitates merging the gas flow field better than other scenarios.

The characteristics of the continuous phase are to determine the quality of the breakup process. Therefore, understanding the gas dynamic behavior is extremely significant. The axial velocity is the major component of gas velocity variable in the free-fall swirling gas atomizer. Figure 3.13 displays the gas axial velocity variations at various stand-off distances, z=5-11 cm for β=$4°$-7° with the same radial angle of $14°$. It shows that for the case of β=$4°$, there is a backward flow between the gas jets at z=5 and 7 cm, while the focal point is located at around z=5 cm. It confirms that the breakup process is accompanied by reverse flow exactly at the point that it starts to take place. This could be the convincing reason for any splash of melt drops on the gas nozzle tip which is followed by the interruption in proceeding the atomization process. Furthermore, a quite slighter back stream between the gas jets can be found for the case of β=$5°$ as well at the axial distances of 5 and 7 cm; but, for this case, the focal point is situated right after z=7 cm. Hence, the existing reverse flow can not disrupt the breakup process. In contrast to the case of β=$4°$ and $5°$, there is no clue of backward stream in the cases of β=$6°$ and 7° in which the breakup occurs at z=9 and 10 cm, respectively.

The sleeve feature which is proposed by this work, is mainly for delivering the melt stream

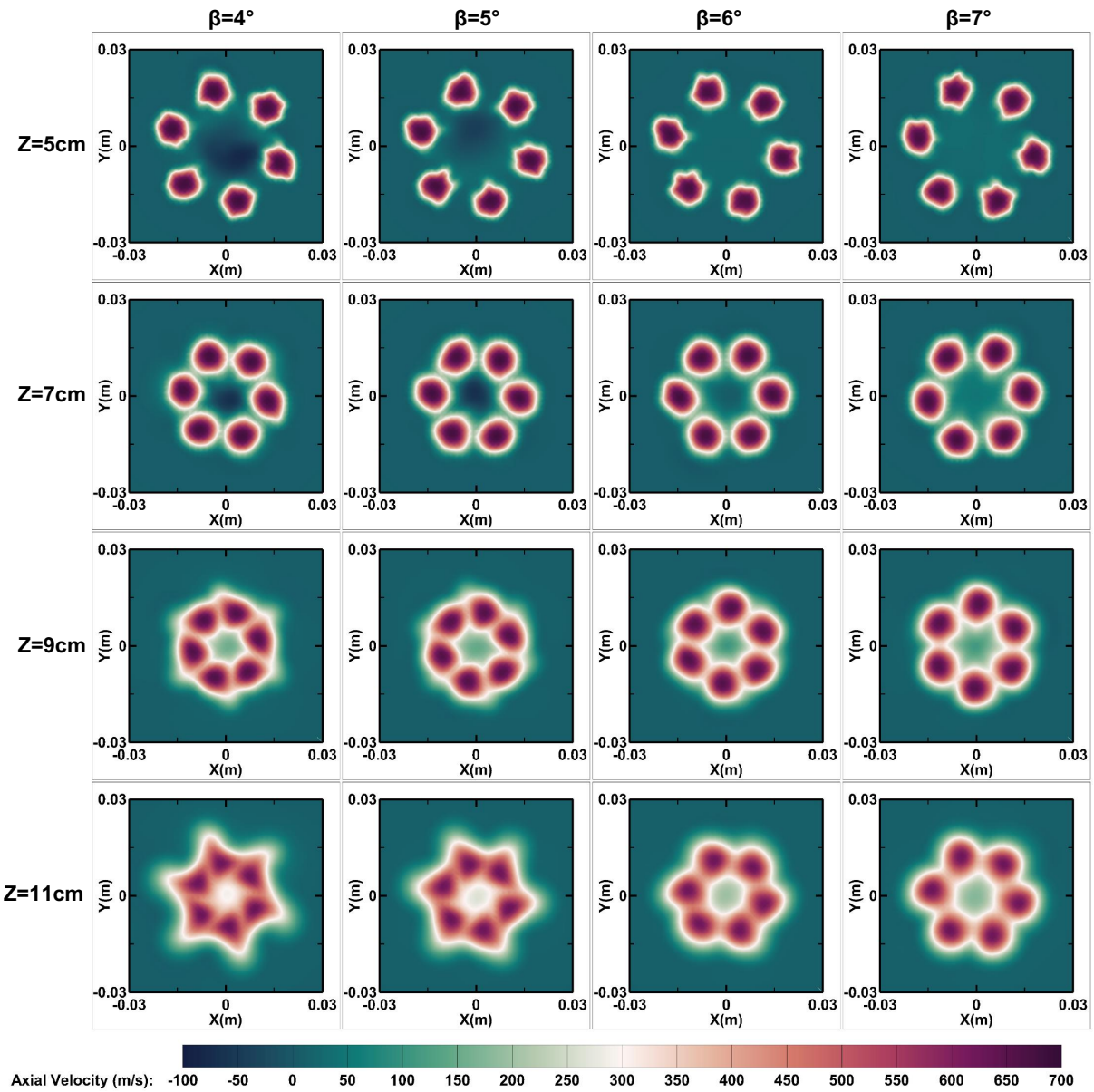

Figure 3.13: Gas axial velocity fields in different stand-off distances from the melt exit versus various swirl angles with the same radial angle of 14°.

right to the focal point. It could be helpful to avoid the interruption of backward flow, however, in the case of β=4°, the gas jets meet the molten liquid flow so closely to the gas nozzle exits.

Figure 3.14 shows the influence of variation in the swirl angle versus PSD and cumulative

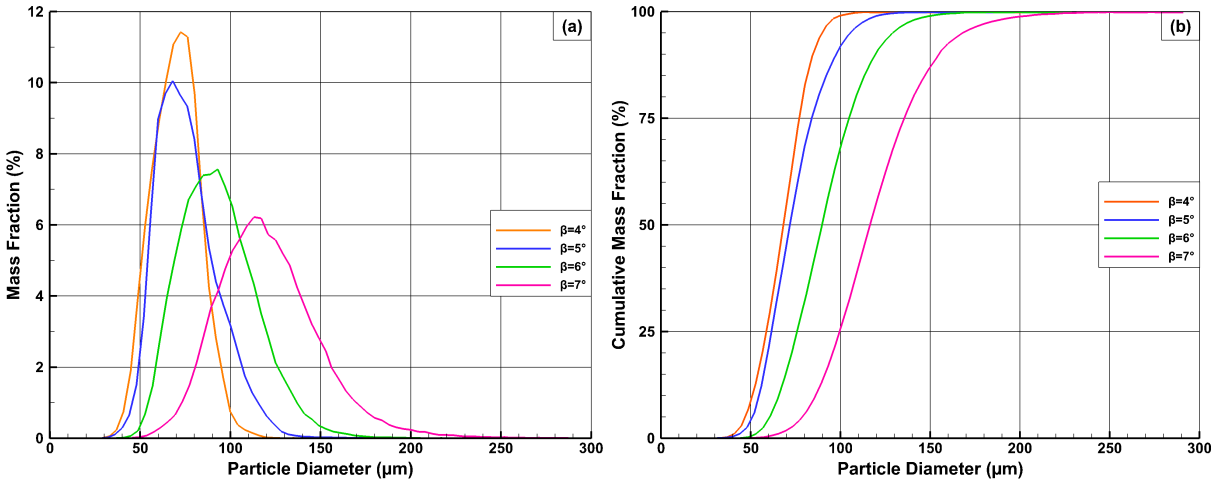

Figure 3.14: Effect of change in the swirl angle on the PSD and cumulative particle size distribution of 6-nozzle die under the same operating condition.

particle size distribution for the cases of β=4°-7° under the same continuous- and dispersed-phase condition. As can be observed, the mass fraction percentage of the peak of PSD is inversely proportional to the swirl angle. Decreasing the swirl angle results in shifting the PSD to the left side for all cases except for β=4°. As explained in detail in Fig. 3.12 and Fig. 3.13, it can be rooted in the developed backward flow around the focal point and merging the gas flow fields that leads to leaving no room between the gas jets for passing the melt stream. Overall, the reduction in the swirl angle makes the PSD narrower and produces smaller particle median diameter.

Chapter 4

Conclusion and future work

Overview

In this chapter, the conclusion of this investigation is presented and future work for numerical and experimental studies in the free-fall swirling gas atomization process are proposed.

The present work was undertaken to simulate the interactions between a compressible turbulent gas flow and superheated molten metal stream in free-fall swirling gas atomizers using a two-way coupled Eulerian-Lagrangian approach. This work numerically analyzed the influence of process parameters and design factors on the particle size distribution and mass median diameter (d_{50}). The numerical results show that the arrangement of gas nozzles is crucial for harvesting the gas energy to destabilize the melt stream efficiently. In comparison with the conventional free-fall design, the free-fall swirling layout features an extra angle, tangential angle (β), with respect to the focal area creating the swirl motion of gas jets around the melt stream. This configuration brings the focal point to a point closer to the die body, contributing to benefiting the most from the gas phase kinetic energy, introducing azimuthal disturbances, and avoid the gas nozzles to get clogged.

The key process variables, including gas-to-melt ratio, number of gas nozzles, and parent droplet size, were examined through various scenarios. The greater GMR and number of nozzles may lead to form smaller sized molten drops, meaning the particle size distribution becomes narrower with smaller d_{50}. On the other hand, any changes in parent drop size in the order of millimeter has no significant effect on the resulting particle size distribution.

The design factors, i.e. radial and swirl angles were also studied qualitatively and quantitatively. According to the results, the molten metal stream is much more shed if the radial angle is increased. However, this trend is repeated when the swirl angle decreases at the same radial angle. The reduction of swirl angle could be beneficial up to a certain angle under two considerations. Firstly, the swirl motion of gas flow would be able to surround and disintegrate the melt stream with the largest-velocity flow field; secondly, no back flow would be formed around the impingement zone. Optimizing the radial and swirl angles might be obtained by the trial and

error method in the large-scale production plants.

The free-fall swirling gas atomization process is a complex multi-physics process. The complexity level of this physical process involves the sensitivity of the angles arrangement, highly supersonic gas flow generation, the interaction between gas and liquid phases, and avoiding the molten metal build-up near the die. Considering all these factors has made it difficult to come up with a global numerical model for the simulation of this process. However, there are some future steps that can be taken to improve the existing model to provide a better understanding of the physics involved in this complicated process. Some of these steps are listed below.

- In this study, the Kelvin-Helmholtz Rayleigh-Taylor (KHRT) breakup model is employed to simulate the secondary breakup process. The option of combined volume of fluid (VOF) and DPM models will allow us to analyze both primary and secondary breakup processes. When the molten metal is injected to the atomization chamber, the liquid column can be modeled using the VOF method and after the disintegration zone, the particles can be tracked using the DPM model.

- Regarding the swirl motion of the gas flow, the large eddy simulation (LES) turbulence model can be used to capture the recirculation flow and vortex structure in detail. It should be noted that the mesh generation can be further optimized to reduce the computational costs of the LES turbulence model.

- The compressible supersonic gas flow is developed through converging-diverging nozzles. The impact of gas nozzle geometry on the delivered gas velocity field to the atomization zone and particle size distribution can be considered as a potential future work.

- The atomizer could be designed and fabricated in such a way that the gas nozzles would

have that freedom to be oriented in the desired directions. It provides a better understanding of the angles arrangement and melt built-up on the atomizer body experimentally.

- Throughout this investigation, it is assumed that the particles are spherical during the entire disintegration process. Future studies can be conducted on the particle shape and morphology for a variety of metals and alloys.

Bibliography

[1] A. Lawley, "Atomization: the production of metal powders," *Metal Powder Industries Federation, 1105 College Rd. East, Princeton, New Jersey 08540-6692, USA, 1992. 159*, 1992.

[2] L. V. Antony and R. G. Reddy, "Processes for production of high-purity metal powders," *Jom*, vol. 55, no. 3, pp. 14–18, 2003.

[3] S. Naboychenko, I. Murashova, and O. Neikov, "Handbook of non-ferrous metal powders: Technologies and applications," 2009.

[4] N. Zeoli, H. Tabbara, and S. Gu, "Cfd modeling of primary breakup during metal powder atomization," *Chemical engineering science*, vol. 66, no. 24, pp. 6498–6504, 2011.

[5] A. M. Mullis, A. P. A. Kumar, and D. J. Borman, "Cfd modelling of high pressure gas atomization of liquid metals," in *TMS Annual Meeting & Exhibition*. Springer, 2018, pp. 77–84.

[6] A. S. Baskoro, S. Supriadi *et al.*, "Review on plasma atomizer technology for metal powder," in *MATEC Web of Conferences*, vol. 269. EDP Sciences, 2019, p. 05004.

[7] W. Hopkins, "Fine powder! close-coupled or open-die atomization?" *Metal Powder Report*, vol. 45, no. 1, pp. 41–42, 1990.

[8] A. J. Yule and J. J. Dunkley, *Atomization of melts for powder production and spray deposition*. Oxford University Press, USA, 1994, no. 11.

[9] D. Singh and S. Dangwal, "E ffects of process parameters on surface morphology of metal powders produced by free fall gas atomization," *Journal of materials science*, vol. 41, no. 12, pp. 3853–3860, 2006.

[10] D. Beckers, N. Ellendt, U. Fritsching, and V. Uhlenwinkel, "Impact of process flow conditions on particle morphology in metal powder production via gas atomization," *Advanced Powder Technology*, vol. 31, no. 1, pp. 300–311, 2020.

[11] N. Vogl, H. Odenthal, M. Hüllen, M. Luh, I. Roisman, and C. Tropea, "Physical and numerical modeling of close-coupled atomization processes for metal powder production," *METEC&ESTAD*, vol. 24, no. 28.06, p. 2019, 2019.

[12] H. Kuhn, *Powder metallurgy processing: the techniques and analyses*. Elsevier, 2012.

[13] R. Kaiser, C. Li, S. Yang, and D. Lee, "A numerical simulation study of the path-resolved breakup behaviors of molten metal in high-pressure gas atomization: With emphasis on the role of shock waves in the gas/molten metal interaction," *Advanced Powder Technology*, vol. 29, no. 3, pp. 623–630, 2018.

[14] R. M. German, "Powder metallurgy science," *Metal Powder Industries Federation, 105 College Rd. E, Princeton, N. J. 08540, U. S. A, 1984. 279*, 1984.

[15] U. Fritsching and V. Uhlenwinkel, “Hybrid gas atomization for powder production,” *Powder Metallurgy*, pp. 99–124, 2012.

[16] O. Hongwu, C. Xin, Y. Wentao, and H. Baiyun, “Progress and prospect on the gas atomization,” *PM TECHNOLOGY-CHINA-*, vol. 25, no. 1, p. 53, 2007.

[17] X.-g. Li and U. Fritsching, “Process modeling pressure-swirl-gas-atomization for metal powder production,” *Journal of Materials Processing Technology*, vol. 239, pp. 1–17, 2017.

[18] J. S. Thompson, O. Hassan, S. Rolland, and J. Sienz, “The identification of an accurate simulation approach to predict the effect of operational parameters on the particle size distribution (psd) of powders produced by an industrial close-coupled gas atomiser,” *Powder Technology*, vol. 291, pp. 75–85, 2016.

[19] O. Aydin and R. Unal, “Experimental and numerical modeling of the gas atomization nozzle for gas flow behavior,” *Computers & Fluids*, vol. 42, no. 1, pp. 37–43, 2011.

[20] N. Zeoli and S. Gu, “Numerical modelling of droplet break-up for gas atomisation,” *Computational Materials Science*, vol. 38, no. 2, pp. 282–292, 2006.

[21] D. Singh, S. Koria, and R. Dube, “Velocity of gas from free fall type atomisers,” *Powder metallurgy*, vol. 42, no. 1, pp. 79–85, 1999.

[22] A. Ünal, “Effect of processing variables on particle size in gas atomization of rapidly solidified aluminium powders,” *Materials Science and Technology*, vol. 3, no. 12, pp. 1029–1039, 1987.

[23] D. Singh, A. Tomar, and K. Ojha, "Momentum and heat transfer in gas atomization of melts," *steel research international*, vol. 78, no. 3, pp. 241–247, 2007.

[24] D. A. Firmansyah, R. Kaiser, R. Zahaf, Z. Coker, T.-Y. Choi, and D. Lee, "Numerical simulations of supersonic gas atomization of liquid metal droplets," *Japanese Journal of Applied Physics*, vol. 53, no. 5S3, p. 05HA09, 2014.

[25] A. M. Mullis, N. J. Adkins, Z. Aslam, I. McCarthy, and R. F. Cochrane, "Close-coupled gas atomization: High-frame-rate analysis of spray-cone geometry." *International Journal of Powder Metallurgy*, vol. 44, no. 1, 2008.

[26] S. Motaman, A. M. Mullis, R. F. Cochrane, I. N. McCarthy, and D. J. Borman, "Numerical and experimental modelling of back stream flow during close-coupled gas atomization," *Computers & Fluids*, vol. 88, pp. 1–10, 2013.

[27] S. P. Mates and G. S. Settles, "A study of liquid metal atomization using close-coupled nozzles, part 1: Gas dynamic behavior," *Atomization and Sprays*, vol. 15, no. 1, 2005.

[28] H. Lohner, C. Czisch, and U. Fritsching, "Impact of gas nozzle arrangement on the flow field of a twin fluid atomizer with external mixing," in *Int. Conf. on Liquid Atomization and Spray Systems*, 2003.

[29] H. Lohner, C. Czisch, P. Schreckenberg, U. Fritsching, and K. Bauckhage, "Atomization of viscous melts," *Atomization and Sprays*, vol. 15, no. 2, 2005.

[30] J. Thompson, "A study of process variables in the production of aluminium powder by atomization," *Journal of the Institute of Metals*, vol. 74, no. 6, p. 101, 1948.

[31] D. Singh, S. Koria, and R. Dube, "Study of free fall gas atomisation of liquid metals to produce powder," *Powder metallurgy*, vol. 44, no. 2, pp. 177–184, 2001.

[32] J. B. See and G. H. Johnston, "Interactions between nitrogen jets and liquid lead and tin streams," *Powder Technology*, vol. 21, no. 1, pp. 119–133, 1978.

[33] S. Moir and H. Jones, "The gas velocity profile of a free fall atomizer and its relation to solidification microstructure of collected spray droplets of 2014 aluminium alloy," *Materials Science and Engineering: A*, vol. 173, no. 1-2, pp. 161–164, 1993.

[34] S. Moir, H. Jones, and S. Beck, "Gas velocities from free fall gas atomiser," *Powder metallurgy*, vol. 39, no. 4, pp. 271–274, 1996.

[35] X. Yu, M. Zhao, and G. Zhao, "Influence of atomising gas pressure on 63a solder powder in supersonic atomisation," *Powder metallurgy*, vol. 47, no. 2, pp. 200–204, 2004.

[36] D. Singh, "Development of operating pressure diagram for free fall gas atomization of liquid metals," *ISIJ international*, vol. 43, no. 12, pp. 2067–2069, 2003.

[37] U. Fritsching and K. Bauckhage, "Investigations on the atomization of molten metals: The coaxial jet and the gas flow in the nozzle near field," *PHOENICS Journal of Computational Fluid Dynamics*, vol. 1, no. 5, 1992.

[38] C. Czisch and U. Fritsching, "Flow-adapted design option for free-fall atomizers," *Atomization and Sprays*, vol. 18, no. 6, 2008.

[39] D. Schwenck, N. Ellendt, L. Mädler, J. Fischer-Bühner, P. Hofmann, and V. Uhlenwinkel, "Generation of small batch high quality metal powder," *Powder metallurgy*, vol. 57, no. 3, pp. 171–175, 2014.

[40] A. Fluent, "19.2 theory guide; ansys," *Inc.: Canonsburg, PA, USA*, 2018.

[41] C. K. Batchelor and G. Batchelor, *An introduction to fluid dynamics*. Cambridge university press, 2000.

[42] D. R. Lide, *CRC handbook of chemistry and physics*. CRC press, 2004, vol. 85.

[43] J. J. Valencia and P. N. Quested, "Thermophysical properties," 2013.

[44] L. Talbot, R. Cheng, R. Schefer, and D. Willis, "Thermophoresis of particles in a heated boundary layer. 101," 1980.

[45] J. Brillo and I. Egry, "Surface tension of nickel, copper, iron and their binary alloys," *Journal of materials science*, vol. 40, no. 9-10, pp. 2213–2216, 2005.

[46] F. Jabbari, M. Jadidi, R. Wuthrich, and A. Dolatabadi, "A numerical study of suspension injection in plasma-spraying process," *Journal of thermal spray technology*, vol. 23, no. 1-2, pp. 3–13, 2014.

[47] K. Pourang, C. Moreau, and A. Dolatabadi, "Effect of substrate and its shape on in-flight particle characteristics in suspension plasma spraying," *Journal of Thermal Spray Technology*, vol. 25, no. 1-2, pp. 44–54, 2016.

[48] C. Crowe, "Drag coefficient of particles in a rocket nozzle." *AIAA Journal*, vol. 5, no. 5, pp. 1021–1022, 1967.

[49] R. Clift, J. R. Grace, and M. E. Weber, *Bubbles, drops, and particles*. Courier Corporation, 2005.

[50] P. Saffman, "The lift on a small sphere in a slow shear flow," *Journal of fluid mechanics*, vol. 22, no. 2, pp. 385–400, 1965.

[51] W. Zhao, F. Cao, Z. Ning, G. Zhang, Z. Li, and J. Sun, "A computational fluid dynamics (cfd) investigation of the flow field and the primary atomization of the close coupled atomizer," *Computers & chemical engineering*, vol. 40, pp. 58–66, 2012.

[52] M. Pilch and C. Erdman, "Use of breakup time data and velocity history data to predict the maximum size of stable fragments for acceleration-induced breakup of a liquid drop," *International journal of multiphase flow*, vol. 13, no. 6, pp. 741–757, 1987.

[53] N. Ashgriz, *Handbook of atomization and sprays: theory and applications*. Springer Science & Business Media, 2011.

[54] M. Jadidi, M. Mousavi, S. Moghtadernejad, and A. Dolatabadi, "A three-dimensional analysis of the suspension plasma spray impinging on a flat substrate," *Journal of Thermal Spray Technology*, vol. 24, no. 1-2, pp. 11–23, 2015.

[55] C. T. Crowe, J. D. Schwarzkopf, M. Sommerfeld, and Y. Tsuji, *Multiphase flows with droplets and particles*. CRC press, 2011.

[56] L. L. Kavanau and R. Drake Jr, "Heat transfer from spheres to a rarefied gas in subsonic flow," California Univ Berkeley Inst Of Engineering Research, Tech. Rep., 1953.

[57] K. Pourang, “Effect of substrate on in-flight particle characteristics in suspension plasma spraying,” Ph.D. dissertation, Concordia University, 2015.

[58] E. Dalir, C. Moreau, and A. Dolatabadi, “Three-dimensional modeling of suspension plasma spraying with arc voltage fluctuations,” *Journal of Thermal Spray Technology*, vol. 27, no. 8, pp. 1465–1490, 2018.

[59] M. Jadidi, S. Moghtadernejad, and A. Dolatabadi, “Numerical modeling of suspension hvof spray,” *Journal of Thermal Spray Technology*, vol. 25, no. 3, pp. 451–464, 2016.

[60] J. Brillo and I. Egry, “Density determination of liquid copper, nickel, and their alloys,” *International journal of thermophysics*, vol. 24, no. 4, pp. 1155–1170, 2003.

[61] S. Alavi and M. Passandideh-Fard, “Numerical simulation of droplet impact and solidification including thermal shrinkage in a thermal spray process,” in *International Heat Transfer Conference*, vol. 49415, 2010, pp. 731–739.

[62] R. D. Zucker and O. Biblarz, *Fundamentals of gas dynamics*. John Wiley & Sons, 2002.